

Correction and alignment strategies for the beam separator of the PEEM3 microscope

Peter Schmid,* Jun Feng, Howard Padmore, David Robin,

Harald Rose, Ross Schlueter, and Weishi Wan

Lawrence Berkeley National Lab, 1 Cyclotron Road

Mail Stop 80R0114, Berkeley, CA 94720-8229, USA

Étienne Forest

High Energy Accelerator Research Organization,

1-1 Oho, Tsukuba, Ibaraki 305-0810, Japan

Ying Wu

Department of Physics, Duke University, Durham, NC 27708, USA

(Dated: July 1, 2004)

Abstract

A new high-resolution aberration corrected photoemission electron microscope (PEEM3) will be installed on an undulator beam line at the Advanced Light Source (ALS) at the Lawrence Berkeley National Laboratory. The aim of this instrument is to provide a substantial flux and resolution improvement by employing an electron mirror for correcting both the third-order spherical aberration and the primary chromatic aberration. In order to utilize this concept of correction, a beam separator is a prerequisite. Crucial to achieving a resolution of 5 nm for the high resolution mode, and a sixteen-fold increase in throughput at the same resolution as its predecessor, PEEM2, specified as 20 nm at 2 % transmission, for the high flux mode is the double symmetric design of the beam separator, which eliminates all the second order geometric aberrations. Nonetheless, substantial tuning capabilities must be incorporated into the PEEM3 design to compensate for both systematic and random errors. In this paper, we investigate how to correct for non-systematic imperfections and for systematic uncertainties in the accuracy of the magnetic fields and focus on how degradation of the resolution and the field of view can be minimized. Finally, we outline a tentative correction strategy for PEEM3.

PACS numbers: 07.78, 41.85, 42.15.F, 41.75

*Electronic address: poschmid@lbl.gov

I. INTRODUCTION

X-PEEM combines the power of synchrotron radiation spectroscopy with the imaging capabilities of transmission electron microscopy. Soft x-ray radiation with a typical photon energy of $100 - 1000$ eV from a synchrotron radiation source can be tuned through core excitation energies to reveal chemical and magnetic information through changes in the x-ray absorption. This absorption is monitored through the yield of electrons from the material surface, and imaged with full field electron microscopy [1, 2]. Images are acquired at energies spanning an absorption edge, and spectra can then be associated with each individual position on the sample. The position of an x-ray absorption is used to identify the element while variations in the detailed structure at the edge provide information on chemical and electronic state. Differences in the structure at the edge recorded with linearly or circularly polarized light provide information on bond orientation and magnetic state. A spectacular example of the application of such techniques to problems in interfacial magnetism is the coupling of ultra-thin ferromagnetic layers to anti-ferromagnetic substrates by Ohldag and co-workers [3]. The imaging is produced through use of typically a low voltage (20 kV) electrostatic, or electrostatic-magnetic immersion objective lens, and a series of projector lenses.

All X-PEEMs functioning today are based on this simple concept and are not aberration corrected. Their resolution is therefore limited by both spherical and chromatic aberrations. The spherical aberration is reduced by accelerating the electrons to high energy immediately on leaving the sample, thereby reducing the angular spread of the emitted beam. The chromatic aberration results from the thermal distribution of scattered electrons within the sample, extending from 0 eV, peaking at typically 1.5 eV and with a full width of a few eV. The effect of the chromatic source is also reduced by accelerating electrons to high energy. Theoretical and experimental work has shown that the resolution limit for this type of microscope, using synchrotron radiation excitation, is around 20 nm. Going beyond this resolution limit requires aberration correction. Developing an aberration corrected X-PEEM is the main goal of the SMART project in Germany [4] and the PEEM3 project at the Advanced Light Source (ALS) in Lawrence Berkeley National Laboratory. Both systems are based on the findings of Rempfer and co-workers that the inability to cancel terms as predicted under the assumptions of the Scherzer theorem [5] can be avoided by reversing the

direction of electrons in the system with use of an electron mirror [6, 7]. In Rempfer’s work and the work of Preikszas and Rose [8], it was found that an electron mirror could correct the spherical and chromatic aberrations of the accelerating field of an immersion objective lens. However, practical implementation requires separation of the incoming and outgoing rays, coming from the objective, and going to the projector column. This beam separator itself is not rotationally symmetric, so aberrations that it introduces cannot be corrected by the rotationally symmetric mirror; it therefore must be designed and fabricated with aberrations below the values specified for the entire microscope. The route to the system used in SMART and in PEEM3 was first identified by Rose and Preikszas [9] and further developed in the work of Müller et al [10]. This scheme of a combination of immersion lens objective, aberration free separator, electron mirror and projector lens column, although well studied, has yet to demonstrate the theoretical performance of 2 nm resolution. The system is complex; therefore, it requires sophisticated alignment and complex manufacturing techniques.

For reliable and successful operation of the PEEM3 microscope, the influence of field deviations from design values must be studied and compensated. In this paper, we will investigate how non-systematic imperfections and systematic errors in the beam separator, which is the most sensitive and critical electron optical element, give rise to aberrations and thus degrade image quality. The insights gained from these studies lead to specifications for the machining tolerances and a correctable range for errors. Furthermore, the findings suggest an alignment strategy for the aberration corrector.

Optical components of the corrected microscope are outlined in Section II, perturbations that can arise in the beam separator are summarized in Section III, and mitigation measures are outlined. In Section IV we outline an alignment strategy for the aberration corrector of PEEM3. Finally, in the Sections V and VI, separators hampered by the perturbations mentioned herein are modeled numerically and how these deviations affect the resolution, the field of view, and the operation of the electron optics are documented.

II. OUTLINE OF THE PEEM3 MICROSCOPE

The full view of the PEEM3 microscope which will be installed on undulator beam line 11.0.1 at the ALS is shown in Figure 1. It will be fastened to a heavy granite block with

mechanical dampers to reduce the mechanical vibrations. The linear dimensions of the system are $190\text{ cm} \times 125\text{ cm}$.

The electron optical components of PEEM3 are depicted in Figure 2. The photons, typically soft X-rays with an energy of $100 - 1000\text{ eV}$, impinge from the left into the sample chamber residing in UHV. Photoelectrons generated are focused by a purely electrostatic immersion lens which also accelerates the electrons to 20 kV .

The axial aberration correction mechanism is provided by an electrostatic tetrode mirror in combination with a magnetic beam separator. The tetrode mirror provides adjustable voltages on three of its electrodes. They are necessary for adjusting the refraction power of the mirror and for nulling the coefficients of both spherical aberration C_S and chromatic aberration C_C of the objective lens.

In order to utilize the correcting properties of an electron mirror, incident electrons must be separated from those reflected. For this purpose a beam separator is required, which does not introduce any new performance-limiting aberrations. This is achieved by a separator with a double symmetric path of rays, removing all second-order geometric aberrations.

Two field lenses are located at intermediate image planes, one lens in front of and the other behind the separator. They are used for adjusting the field rays independently from the axial rays in such a way that off-axis coma is eliminated. Eliminating this aberration is important because it limits the field of view and, hence, may severely hamper the usability of the corrected electron microscope.

After the electron beam passes through the separator for the second time (a second 90° pass), it forms an image of the diffraction plane at the back focal plane of the transfer lens. In this plane a diaphragm limits the aperture angle without affecting the field of view. Finally, the beam is magnified by the projector system to the final image plane, where the image is recorded by a CCD camera.

In addition to the electron optical elements mandatory for a corrected PEEM, we implement additional devices for adjusting, steering and monitoring the PEEM. These are discussed in detail in Sections III and IV. There are two electrostatic dodecapole elements directly behind the objective lens. In front of the beam separator are two combined electromagnetic twelve-pole elements in the mirror arm. Another electrostatic twelve-pole element is located at the exit of the beam separator. Twelve-pole elements were chosen as correction devices for parasitic aberrations which are caused by small mechanical or electrical imper-

fections in the lenses since they are able to generate dipole, quadrupole and hexapole fields of any desired azimuthal orientation, allowing the correction of displacement, twofold astigmatism, and threefold aberrations. These twelve-pole elements do not introduce parasitic aberrations lower than fifth order. In addition, excitation of an octopole field is possible.

At certain planes, beam monitoring and analyzing devices can be inserted into the optical path. In the proximity of the separator’s image planes pinholes and coded grids can be placed allowing sophisticated beam diagnostics. For analyzing the beam after a single pass through the separator a “90° PEEM” facility is provided. This configuration comprises a fully functional PEEM including all the optical components of PEEM3 from the sample through the mirror. In this configuration the second field lens is used in a different imaging mode and the mirror is effectively turned off. The beam passes through a hole in the mirror provided for optical alignment and the image is recorded by a separate CCD camera. This tool, dedicated for monitoring the status of the separator alignment, will help us in learning how the separator can be operated, leading to subsequent semi-automatic computer controlled monitoring and alignment of the microscope.

III. IMPERFECTIONS AND CORRECTION STRATEGIES

Paramount to successful aberration correction is that the setup of the separator magnets realizes as many symmetries as possible. We impose three symmetries on the ideal layout. The first symmetry is the midsection symmetry of the separator in the y -direction, which is mandatory to achieve the planar optic axis necessary to avoid introducing torsion. This trait reduces the number of excited aberration coefficients considerably, making the numerical calculation practical. The second and third symmetries comprise double-symmetry along the optic axis imposed on the path of the fundamental rays leading to the double-symmetric separator layout as shown in Figure 3. The S_1 -symmetry, imposed at the 45° plane, is necessary for nulling many aperture aberration coefficients as well as the second order axial geometrical aberrations, and thus is crucial for achieving good axial resolution. The remaining second order aberrations, proportional to the lateral initial coordinates, vanish because of the symmetry imposed at the 22.5° planes, thereby, securing a large field of view.

Our goal is to maintain the symmetries mentioned above to the greatest extent possible. The main task is to figure out how such a breach will cause a degradation of image quality

and how to monitor that the path of rays in fact keeps the symmetries. When analyzing imperfections and errors, the focus will be to determine their affects on the symmetries and means to adjust for such deviations.

Our concern is to conserve the resolution over a large field of view and to avoid any residual dispersion on the far side of the separator. Residual lower-order aberrations can excite large higher-order aberrations due to coupling with the aberrations of the mirror. Additionally, the displacement of the optic axis of the separator with respect to the axis of the lenses should be minimized. Otherwise the off-central traverse may cause severe deterioration of image quality.

A separator magnet when physically constructed can deviate from the ideal optimized design due to various errors. The errors can be classified in the following categories:

- systematic errors, constrained by the allowed symmetries, such as errors in the magnetic model used throughout the numerical calculations to define the “supposedly” optimized ideal design, or symmetrical fabrication imperfections deviating from the specified design, and
- random errors, such as deviations from the specified groove positions due to non-systematic machining errors, material inhomogeneities, or mechanical misalignment.

Furthermore, deflection and mis-focusing errors of the entering electron beam with respect to the separator—which have nothing to do with the design or imperfections of the separator itself—can give rise to parasitic aberrations, such as defocusing and two-fold axial astigmatism.

A systematic error of particular concern is that of incorrectly specified groove positions caused by either slight three-dimensional geometrical deviations from the assumed two-dimensional Schwartz-Christoffel numerical field model or by deviations from infinite magnetic permeability in the pole material. This subject is addressed in Section V. Furthermore, there can be imperfections caused by systematic machining errors. These systematic errors can be minimized by a thorough analysis of the processes involved in manufacturing the separator pole plates. Note that systematic errors do not break the symmetry of the layout of the separator magnet.

Random imperfections arise due to variations of critical dimensions beyond the control of manufacturing machines and processes. By adhering to the tightest tolerances possible, the

effect of these errors can be minimized. In Section VI we determine the accuracy to which the grooves have to be manufactured so that the errors caused by random deviations from the nominal values can be compensated for by correction elements. In Section VIA we discuss the Gaussian optics and how the dispersion terms can be adjusted by internal correctors. In Section VIB we show how additional external multipole fields generated by twelve-pole elements can be used for correction – dipole fields for orbit control and quadrupole fields for focusing correction.

Of course, there is a limit to the number and magnitude of random errors that can be corrected to a suitable level. For example, compensating for significant deviations from the specified properties of the magnetic material, such as widespread local inhomogeneities, is problematical. The most effective approach is to simply process the material in a stressless way on a best effort basis. If there are perceivable deviations in the alloy giving rise to local permeability non-uniformities then this material is not usable.

Deflection and mis-focusing errors due to a mismatch of the entering beam and the separator can, at least in principle, be removed by beam tuning and focusing. Given the complexity of the separator and the mirror corrector, sophisticated probing and monitoring capabilities are necessary to assess the status of the apparatus and ultimately to correct for component misalignment in a semiautomatic fashion. The monitoring and probing facilities of PEEM3 are shown in Figure 4.

Image planes are located at the entrance and the exit face of the separator. Pin holes and coded grid structures are placed at these planes for determining the position and the orientation of the electron beam. The grids also allow identification of parasitic aberrations. In the mirror column there is the 90° PEEM facility, which allows monitoring of the image after a single pass through the separator, which can aid in understanding how the separator is performing. Two orthogonal dipole deflectors are located at the 45° planes inside of the separator, one deflects in the horizontal plane, the other in the vertical direction. This facility allows us to check whether there is a stigmatic image at these symmetry planes.

IV. SKETCH OF AN ALIGNMENT STRATEGY FOR PEEM3

Because of the inherent complexity of the separator, a feasible alignment strategy is of great importance for operating the microscope. The suppression of various aberrations in

the separator critically depends on the double-symmetry of its design. Deviations from this symmetry can be identified easily because they introduce additional characteristic aberrations [11]. An alignment strategy, which corrects for deviations according to their respective orders, has been developed to restore this double symmetry in the separator optics.

Correcting the aberrations of a given order by multipoles does not affect lower-order ones. Thus the alignment achieved by compensating for errors of lower orders is not affected because a multipole of multiplicity m only affects aberrations of order $n \geq m - 1$.

In the first step, the objective lens, the mirror, and the field lenses are adjusted for an image as sharp as possible on the CCD camera of the 90° PEEM facility.

In the second step, the internal trim current correctors in the separator magnet are adjusted such that a total 90° bend of the separator is achieved as well as zero total lateral and angular dispersion at the exit of the separator. Any lateral displacement induced by the correction elements can be removed by exciting dipole components inside the two combined electro-magnetic twelve-pole elements of the mirror column.

The fundamental axial rays x_α and y_β can be controlled by tuning the focal length of the objective lens. We compensate for the remaining astigmatism by exciting quadrupole fields on the twelve-pole elements in the objective column. The dipoles at the 45° plane are crucial for checking the proper adjustment of the fundamental axial rays; the image plane is determined to be at the midplane of this dipole if changing its setting does not move the beam image at the detecting CCD camera at 90° . Subsequently, the round lenses are adjusted to yield the sharpest image possible.

The field rays x_γ and y_δ can be manipulated by the field lenses in such a way that they intersect the optic axis at the 22.5° planes forming an image of the diffraction plane. Since these lenses are placed near intermediate images, adjusting the field rays does not affect the preceding alignment of the axial rays. Currently, we are investigating how to install deflectors at the 22.5° planes without risking the full operativeness of the separator.

To minimize the deviations from a symmetric path of rays and thus the field aberrations, we impose telescopic conditions on both of the field rays at the entrance and the exit of the separator. In our present design the field rays cannot be manipulated independently from the axial rays without embarking on delicate manipulations involving at least two quadrupole fields. An alternative, straightforward way to adjust the field rays individually is by superposing an additional quadrupole field on the field lenses placed at intermediate

images of the object plane. This can be achieved by subdividing the central electrode of these lenses into segments to provide a quadrupole field with the appropriate orientation. A criterion for achieving a double symmetry is that all the second-order aberrations vanish. If none are present, we can be sure that the field rays are properly adjusted.

How to align for correction of aberrations higher than the second rank will be the subject of another study.

V. CORRECTING FOR SYSTEMATIC ERRORS CAUSED BY IMPERFECTIONS IN THE MAGNETIC FIELD MODEL

As shown in [10, 12], calculating the optical properties of the beam separator accurately is rather involved. In addition to the complexity of the system given by the double symmetry along a curved axis, the positions of the cardinal elements (the image and object focus and the principal planes) and the trajectory of the optic axis must be known to a high degree of accuracy. These properties are sensitive to the assumptions made while developing the field model for the separator magnet. It is essential that the field model for the separator magnet accurately reflects to a sufficient degree that actually present in the as-built device. Unfortunately, there is no exact three dimensional analytic solution for the magnetic fields generated by coils buried in three adjacent curved grooves. Furthermore, all analytic solutions assume isopotential sections at the surface of the pole plate, which is only an approximation given that the permeability of the magnetic material is not infinite.

For computing aberration coefficients, both SMART and PEEM3 designs employ a two-dimensional magnetic field model generated by currents buried deep within grooves, first solved via a Schwartz-Christoffel mapping by Herzog [13]. The geometry of this two-dimensional arrangement is shown in Figure 5. Here, the magnetic field is calculated assuming a pair of excited parallel pole plates of infinite extent in the third dimension, placed symmetrically about the ξ -axis with a gap separation of D . To obtain a well defined decrease of the fringe field, one places two plane-parallel mirror plates at a distance S in front of the pole plates, as shown in Figure 5. The distance of the plates D is the same as that of the pole plates. This calculation assumes that the magnetic potential ψ is constant on the surface of the pole plate.

The magnetic field $B(\xi) = B_y(y = 0, \xi)$ of a Schwartz-Christoffel magnet in the symmetry

section $y = 0$ is given in the most simple form [11] by

$$B(\xi) = \frac{B_0}{2} \left(\frac{\tau}{r} + \sqrt{\frac{1+\tau^2}{1+r^2}} \right), \quad r = \frac{S}{D}, \quad -r \leq \tau \leq r. \quad (1)$$

The auxiliary variable τ is given by

$$\frac{\pi\xi}{D} = r \arctan \tau + \operatorname{arctanh} \left(\frac{\tau}{r} \right). \quad (2)$$

Both calculations in [12, 14] use the field model given by Equation (1) for computing the contribution of a single groove to the total magnetic field. The total magnetic field was obtained either by linearly superposing the contributions of all the grooves, assuming the Schwartz-Christoffel magnet model for each of the grooves [14] or by linearly superposing the fields from each of the two grooves closest to the point of the observation considered in isolation [12].

However, due to groove curvature and depending on the curvature distance to gap ratio, calculations which are solely based on the two dimensional field model may not predict the trajectory of the optic axis with sufficient precision to obtain 2 nm resolution [10]. A different model, using dipole charge sheets, allowing three-dimensionality, was used by SMART to give presumably more accurate values for their groove orientations [10]: The deviations between the two results are 3.9 mrad and 2.3 mrad, respectively, for the orientations of the second and the third groove. Nevertheless, these exceeded the correctable range given by the trim coils of the SMART separator. It turns out that the curvature of the wires and the effect of overlapping fringe fields cannot be neglected for their layout of the separator magnet. The calculations in [10] used as design parameters an edge length of 28 cm, three grooves per symmetry unit with widths of 3 mm, 6 mm and 3 mm, and a full distance of 7 mm between the pole plates.

Although SMART's refined model uses a sophisticated scheme of virtual dipole layers and extrapolation techniques, the magnetic field obtained is still only an approximation to the actual field, because this model ignores the non-infinite permeability of the material used for the pole plates and it relies on a numerical integration, which may also introduce errors. Thus far, the resolution of the SMART mirror corrector employing a separator manufactured according to the specification given by this calculation has only been tested to the 10 nm level [15].

Because of these uncertainties, we did not embark on developing a more sophisticated magnetic field model, but considered ways to improve the matching between the actual and the computed field by changing the parameters of the separator and by investigating methods for correcting symmetric perturbations of the groove orientations. Specifically, we modify our original seven millimeter gap design to a five millimeter design.

Inspecting the formula (1), leads to the conclusion that for a fixed groove width S , the normalized field B/B_0 will decrease more rapidly axially if the gap D between the pole plates is decreased. A faster spatial decay gives rise to a more localized field which means less overlap between of the fields generated by adjacent wires. More importantly, the reduced gap makes the field in the neighborhood of the trajectory more perfectly two-dimensional, thereby the Schwartz-Christoffel model more accurately reflects reality (to perhaps six significant figures rather than four.)

Dipole decay in the vicinity of a groove as a function of the half distance $h = D/2$ of the pole plates is shown in Figure 6 and Table I. The change from $h = 3.5$ mm to $h = 2.5$ mm has dramatic consequences. Whereas at a distance of -10.5 mm from the center of the groove the normalized magnetic field B/B_0 has decayed to 10^{-4} for a seven millimeter gap, it is at the 5×10^{-6} level for a distance between the pole plates of 5 mm. For a distance of -13 mm, the normalized magnetic field strengths are 10^{-5} and 10^{-7} for a separation of 7 mm and 5 mm, respectively (See Table I and II).

As a further consequence of the faster decay of the field, the effect of groove curvature is diminished. Since the location χ , the distance from the center of the groove to the location where the groove begins to bend appreciably, is approximately the same for all gap distances investigated after optimization, the relevant quantity χ/h is again increased by the factor $7/5$ to 3.5 when the half gap distance h is decreased from 3.5 mm to 2.5 mm. Thus, the perturbation from the curved part of the groove to the magnetic field at the beam region is down to the 10^{-5} level (see Table I), if we assume a 90° turn of the groove. For the design shown in Figure 3, field perturbation from the curved portions is even less.

Next we address how decreasing the gap affects the optimized groove configuration and the optical properties of the whole separator. As stated in [16], the secondary electron distribution generated by impinging X-rays for many materials can be modeled by the formula

$$\frac{dN}{dE_k} \propto \frac{E_k}{(E_k + W)^4}. \quad (3)$$

Here dN stands for the number of electrons within the kinetic energy range dE_k , and W is the work function of the sample. For our calculations we assume a work function of 5 eV and 27000 macro particles originating from a point on the sample with weights given by the Equation (3). We randomly select 30 values for the emission angles ϕ and θ and the energy width ΔE , respectively. For the acceleration gap a voltage of 20 kV was assumed. The objective lens is modeled by a linear transfer matrix, magnifying the initial distribution by -12 .

Figures 7 and 8 show the resolution as a function of the radius of the field of view. The resolution is computed in the same way as in [12] but with a magnification of -12 . The field of view in both imaging sections remains largely unaffected when the gap between the pole plates is decreased from seven to five millimeters. As could be expected, the distances between adjacent grooves in an optimized design is largely independent of the gap between the pole plates. In fact, a gap change from seven to five millimeters gives rise to a maximum change of a mere 3.5 % in the groove positions as shown in Table II. The optimized angular orientations of the grooves change at most by about 5 % (See Table III).

In addition to the minor geometric changes, the design current driving the coils is reduced considerably from 69.4 A to 47.9 A or roughly to $5/7$ of the original current, as expected from reducing the gap from seven to five millimeters (See Table IV). Since the heat load scales with the square of the current, the energy dissipated is reduced by one-half.

The layout of the entire PEEM3 separator is shown in Figure 3. The width of all grooves is 3 mm. The edge length is 28 cm, as for SMART. The design is based on the double-symmetry of the separator. Areas with opposite magnetic flux are equalized so as to minimize flux path lengths in the (not quite infinite) Permalloy pole plates. Any residual flux is shorted via Permalloy spacers positioned as close to the beam path as possible without disturbing the fields, as shown in Figure 3. The Permalloy has a permeability of 40000 for a magnetic field strength of 25 mT. To dissipate the heat, a hollow core water-cooled copper-tube is positioned parallel to electrical windings.

In addition to the main coils, the separator includes two trim coils in each groove and a pair of deflectors in each of the 45° symmetry planes to diagnose deviations from a symmetric beam path.

Although the reduction in the gap between pole plates will increase the accuracy of our numerical field model, it remains to be seen whether this will be sufficient to operate PEEM3

in a high-resolution imaging mode at a resolution of about 5 nm. Since the field model is based on several assumptions (two-dimensionality, infinite permeability of the pole plates, no random errors), which are only valid to a certain degree, a procedure allowing to correct for uncertainties in the model and for random fabrication or material imperfections has been developed.

Although the layout of the grooves is double-symmetric when the two-dimensional field model is utilized, the actual path of the fundamental rays may be asymmetrical. In the following, we propose a strategy to regain one of the plane-section symmetries of the fundamental rays, thereby accomplishing a good axial resolution, since imposing a single symmetry on these rays with respect to the 45° plane is sufficient to null the axial aberrations of second order [17]. However, a loss in the field of view is expected since the second symmetry, along the S_2 - or 22.5° planes, is perturbed: some of the aberration terms proportional to the lateral initial coordinates are no longer canceled.

The question is to what extent can a breach of the double-symmetry of the fundamental rays incurred by grooves deviating from the truly optimized design be compensated and how does the field of view degrade?

We assume that such deviations are likely to be of the order of those between the two-dimensional Schwartz-Christoffel and the SMART dipole layer model, the latter also being a numerical approximation, and also neglecting deviations of the value of the permeability from infinity.

To elucidate this question, we studied to what extent we could correct for perturbations caused by a mispositioning of the center grooves. The strategy employed was to (a) set up the system double symmetrically, (b) add a perturbation tilt to the second groove and then (c) try to find a solution that maintains a stigmatic image plane at the 45° plane and a symmetric trajectory of the dispersion ray. This gives four constraints: a total bending angle of 45° at the (S_1) plane, with the x_α - and y_β -rays vanishing at that plane, $x_\alpha(z_{S_1}) = y_\beta(z_{S_1}) = 0$, and with the condition $x'_\kappa(z_{S_1}) = 0$. Four parameters we employ for correcting: the three independent trim coil currents, one in each groove – the other trim coil currents are determined by exciting the trims double-symmetrically – and the defocusing (the distance of the image plane from the nominal plane at the edge of the separator).

The results presented in the Figures 9 and 10 show that compensating for design mis-specification of up to $+4/-2.8$ mrad to the center angle is feasible, as the decrease in the field

of view is acceptable in both imaging sections.

This simple correction scheme is not able to accommodate for changes greater than $+4/-2.8$ mrad. More sophisticated schemes incorporating external multipole elements, which do not rely on changes of the optic axis within the separator, are likely to surpass the correctable range given by the strategy outlined above.

VI. RANDOM ERRORS CORRECTION

A. Correcting for a single pass through the separator

In the previous section we outlined how to correct for mis-specifications of the correct groove orientations caused by limitations of our two-dimensional field model. In this section we investigate to what extent random mechanical imperfections can be compensated.

Whereas in a previous study [12] the correction was achieved by artificially setting elements of the linear transfer map to zero, to estimate the impact of aberrations when the Gaussian optics could be brought back to its design values by some hypothetical perfect linear-focusing corrector, in the present study the internal trim correctors currents are utilized for compensation, modeling a realistic means of correction.

Contrary to the correction scheme pursued in the previous Section V, which utilized the trim coil currents to correct double-symmetrically; therefore only three independent correcting currents per 90° turn prevailed; throughout this Section, there is no additional symmetry imposed on the correctors. Thus, six independent currents as variables are available. The six trim coil currents,

$$I_i, \quad i = 1, \dots, 6, \quad (4)$$

are used to adjust four coefficients of the Gaussian optics utilizing the singular-value decomposition technique.

The four quantities, to be corrected, are:

1. $m_{12}(z_E)$, which corresponds to a combination of the defocusing and the axial astigmatism in the x - z section (see Equations 5 and 6);
2. $m_{34}(z_E)$, which corresponds to a combination of the defocusing and the axial astigmatism in the y - z section;

3. $d_x(z_E) = x_\kappa(z_E)$, the angular dispersion; and

4. $d_{p_x}(z_E) = x'_\kappa(z_E)$, the lateral dispersion.

All of these terms are determined at the exit plane of the separator $z = z_E$.

As set of possible misalignment errors we choose $\sigma_{x,y} = 25 \mu\text{m}$ and $\sigma_\phi = 1 \text{ mrad}$ for the positions and orientations of the grooves, respectively. Assuming a Gaussian distribution for the errors in position and in angle with a two standard deviations σ cut, an ensemble of 100 misaligned separators was used for studying the effectiveness of the correction scheme outlined above.

To obtain and analyze the optical properties of misaligned separators, parameter-dependent non-linear transfer maps are generated from the separator design code developed with the Differential Algebra (DA) method. These maps describe the imaging properties as functions of the groove orientations and positions, as well as the magnetic potentials as parameters.

In the studies, the DA maps include aberrations through fourth order and a linear dependence on the geometrical parameters and currents of the main and the correction coils. The six correction currents are set to null the selected aberration terms. The resulting map is then used for tracking the initial particle distribution through one quadrant of the separator, after propagating through the objective lens, which is assumed to be ideal.

The distribution of the random linear aberration coefficients to be corrected are shown in Figure 11. Since for the misalignments a Gaussian distribution was selected, we fitted the histogram of the coefficients to a Gaussian. This gives the center and the standard deviation of the distribution. The correction schemes are aimed to correct 90 % of imperfect separators among the randomly generated ensemble. This 90 % of confidence level translates to the limits at $\pm 1.65\sigma$ assuming a Gaussian distribution as shown in Figure 11.

Although the specifications of the separator are rather tight, they are $25 \mu\text{m}$ for the positions and 1 mrad for the angles: these are non-negligible deviations from the nominal values present. Since the dispersion terms cannot be compensated externally, they must be nulled by the dipole fields within the separator.

The distribution of the corrector strengths relative to the current I_0 driving the main current is shown in Figure 12. The standard deviations for the six currents over I_0 are $\sigma_1 = 0.262 \%$, $\sigma_2 = 0.335 \%$, $\sigma_3 = 0.153 \%$, $\sigma_4 = 0.473 \%$, $\sigma_5 = 0.318 \%$, and $\sigma_6 = 0.243 \%$,

respectively. To remain within the 90 % regime of the distribution, requires a trim of at most 1 % of the main current. Therefore, we expect that the nonlinear part of the imaging will not be substantially affected by the additional aberrations induced by exciting the alignment coils.

The resolutions in the x - z section and the y - z section before and after correction for an axial sample point are shown in Figure 13. On the abscissae the deviations of the resolution from a perfectly aligned and machined system are shown. For a perfect front end with a magnification of -12 the nominal values for the resolutions are $\delta_{x_0} = 0.54$ nm and $\delta_{y_0} = 2.1$ nm for an axial point. The figures clearly demonstrate that the correction scheme works for this point. The deviations from the nominal values for the ensemble of corrected separators is negligibly small. The same is true for an off-axial point as demonstrated in Figure 14. For the point with the coordinates $(-5 \mu\text{m}, -5 \mu\text{m})$ on the sample, the resolution can be recovered sufficiently close to the design values of $\delta_{x_0} = 0.67$ nm and $\delta_{y_0} = 4.3$ nm by correction.

There is a limitation of our correction scheme, however: It is not possible to compensate for a displacement of the center of the distribution in the x -direction, as shown in Figure 15. This shift of some hundred micrometers must be removed externally. We will investigate how this shift influences the image quality in the next section. Of special concern is that an off-axis beam passing through the field lenses might excite degrading aberrations.

B. Correcting for a perturbed separator in an otherwise aligned system with additional external dipole and quadrupole elements

In this subsection, we describe the correction methods using both built-in trim current correctors and external corrector elements. The elements are shown in Figure 4. The electron rays are computed from the sample where they originate with a work function of 5 eV. Subsequently, they are accelerated to 20 kV by the cathode lens and imaged by the objective in a plane in front of the beam separator, where the first field lens is located. After traversing the separator, the electrons enter the mirror which compensates for the spherical aberration and the chromatic aberration of the objective lens and reflects the electrons back to the separator. The angular aperture is set by the aperture at the back focal plane of the transfer lens behind the separator. The resolution as a function of the transmission or the

aperture is calculated at the final image plane following the aperture.

With the exception of the separator, all of the components mentioned above are at their design values. The tolerable misalignments of the separator must not induce errors which are larger than $\sigma_{x,y} = 10 \mu\text{m}$ and $\sigma_\phi = 0.5 \text{ mrad}$. Otherwise the required resolution cannot be obtained by means of the correction procedure. After randomly selecting an ensemble of 500 misaligned separators with the tolerances given above, 27000 particles generated in the same way as in the previous section were tracked from the sample to the first image plane after the aperture.

In the first stage in addition to internal corrections within the separator, dipole elements are excited on the twelve-pole elements in the mirror arm and in front of the transfer lens, to adjust the optic axis. When correcting for lateral deviations of the rays leaving the separator after the first pass, we utilize the fact that the force of a magnetic dipole field is velocity dependent. Thus, we choose equal electric and magnetic dipole strengths. Then the alignment of the incident rays does not affect the pass of the reflected ones. The reflected beam enters the separator on-axis traversing it for the second time.

In the next step, the linear focusing terms are adjusted in the same way by means of electrostatic and magnetic quadrupole fields. To investigate whether there is a correlation between a specific linear focusing term and the resolution, we refer to Figures 16 and 17, where the off-diagonal and diagonal elements of the linear transfer matrix are plotted as spot diagrams. It can be gathered from these figures that a relationship is clearly visible for the m_{12} and m_{34} terms.

These relations become evident by writing the first-order axial aberrations in the form

$$\begin{aligned}\Delta x &= m_{12} x'_0 = (C_1 + A_1) x'_0 \\ \Delta y &= m_{34} y'_0 = (C_1 - A_1) y'_0.\end{aligned}\tag{5}$$

Here we adhere to standard electron optical notation for the defocusing $C_1 = -\Delta f$ and the axial astigmatism A_1 . When these aberration coefficients are nullified, the terms in the spectroscopic notation vanish as well because of the relations

$$\begin{aligned}m_{12} &= C_1 + A_1 \\ m_{34} &= C_1 - A_1.\end{aligned}\tag{6}$$

Therefore we corrected for both of these terms by additional quadrupole fields within the twelve-pole elements, eliminating the axial astigmatism A_1 and the defocus by readjusting

the focal strengths of the objective lens and the mirror. The axial resolution computed before and after correction for the aperture radii of $5\text{ }\mu\text{m}$ and $25\text{ }\mu\text{m}$ is presented in Figure 18.

This figure indicates that the correction scheme allows recovery of the axial resolution computed in radius δ_{r_0} within one standard deviation to the nominal value of 5 nm and 27 nm for an aperture radius of $5\text{ }\mu\text{m}$ and $25\text{ }\mu\text{m}$, respectively.

Finally, the resolution versus transmission curve is plotted for the perfectly aligned system without imperfections in Figure 19. The deviations for the ensemble of separators after correction are shown as error bars. A separator with standard deviations smaller than $\sigma_{x,y} = 10\text{ }\mu\text{m}$ and $\sigma_\phi = 0.5\text{ mrad}$ should allow a successful operation of PEEM3.

VII. CONCLUSIONS

We have decreased the separator gap to 5 mm to increase the accuracy of the two-dimensional field model vis-à-vis the actual field; we have developed effective correction schemes to restore the separator performance for random errors less than $\sigma_{x,y} = 10\text{ }\mu\text{m}$ and $\sigma_\phi = 0.5\text{ mrad}$ and for systematic perturbations of less than $+4/-2.8\text{ mrad}$ of the orientation of the center grooves. With these developments, we expect that the PEEM3 separator will be able to achieve an axial resolution of 5 nm with a sufficient field of view, as long as the symmetry of the fundamental rays at the 45° planes is preserved. Nevertheless, much effort will be invested in developing an on-line monitoring program and a comprehensive alignment strategy for a robust and reliable operation of the aberration correction facility of PEEM3.

Acknowledgments

Work supported by the Director, Office of Energy Research, Office of Basic Energy Sciences, Material Sciences Division, U.S. Department of Energy, under Contract No. DE-AC03-76SF00098

-
- [1] J. Stöhr, H. A. Padmore, S. Anders, T. Stammmler, and M. R. Scheinfein, *Surf. Rev. Lett.* **5**, 1297 (1998).
 - [2] S. Anders, H. A. Padmore, R. M. Duarte, T. Renner, T. Stammmler, A. Scholl, H. R. Scheinfein, J. Stöhr, L. Seve, and B. Sinkovic, *Rev. Sci. Instrum.* **70**, 3973 (1999).
 - [3] H. Ohldag, T. J. Regan, J. Stöhr, A. Scholl, F. Nolting, J. Lüning, C. Stamm, S. Anders, and R. L. White, *Phys. Rev. Lett.* **87**, 1 (2001).
 - [4] R. Fink, M. Weiss, E. Umbach, D. Preikszas, H. Rose, R. Spehr, P. Hartel, W. Engel, R. Degenhardt, R. Wichtendahl, et al., *Journal of Electron Spectroscopy & Related Phenomena* **84**, 231 (1997).
 - [5] O. Scherzer, *Z. Phys.* **101**, 593 (1936).
 - [6] G. F. Rempfer and M. S. Mauck, in *Proc. EMSA meeting*, edited by G. W. Bailey (San Francisco Press, San Francisco, Louisville, KY, 1985), p. 132.
 - [7] G. F. Rempfer, M. S. Fyfield, and O. H. Griffith, *Microsc. Microanal.* **3**, 14 (1997).
 - [8] D. Preikszas and H. Rose, *J. Electron Microsc.* **1**, 1 (1997).
 - [9] H. Rose and D. Preikszas, *Optik* **92**, 31 (1992).
 - [10] H. Müller, D. Preikszas, and H. Rose, *J. Electron Microsc.* **48**, 191 (1999).
 - [11] H. Rose and D. Krah, in *Energy-Filtering Transmission Electron Microscopy*, edited by L. Reimer (Springer, Berlin, Heidelberg, 1995), pp. 43–149.
 - [12] Y. K. Wu, D. S. Robin, E. Forest, R. Schlueter, S. Anders, J. Feng, H. Padmore, and D. H. Wei, *Nuclear Instruments and Methods in Physics Research A* **519**, 230 (2004).
 - [13] R. Herzog, *Zeitschrift für Physik* **97**, 596 (1935).
 - [14] D. Preikszas, Ph.D. thesis, Technische Hochschule Darmstadt, Darmstadt (1995).
 - [15] P. Hartel, D. Preikszas, R. Spehr, H. Müller, and H. Rose, in *Advances in Electronics and Electron Physics*, edited by P. Hawkes (Academic Press, 2002), vol. 120.
 - [16] B. P. Tonner and D. Dunham, *Nuclear Instruments and Methods in Physics Research A* **347**, 436 (1994).
 - [17] S. Lanio, Ph.D. thesis, Technische Hochschule Darmstadt, Darmstadt (1986).

List of Figures

1	Full view of the PEEM3 spectromicroscope.	27
2	The components of the PEEM3 microscope.	28
3	Layout of the separator windings. The double-symmetric layout is clearly visible. Vertical and horizontal dipole elements are located at the 45° planes, intended for checking the location of the image planes.	29
4	Schematic layout of PEEM3. All of the correction and monitoring facilities are indicated. Such as the 90° PEEM facility provided in the mirror column, consisting of the modified field lens F_2 , the mirror, the additional lens P_3 and a separate CCD camera. For external correction, there are the electrostatic decapole elements D_1 through D_7 which can be employed to generate dipole, quadrupole, hexapole and octopole fields to correct for parasitic aberrations. In order to influence the impinging and the reflected beam independently utilizing the velocity dependence of the magnetic component of the Lorentz force, the elements D_3 and D_4 are combined electrostatic and magnetic twelve-pole elements. At the exit and the entry faces of the separator there are coded grids and pinholes which can be moved by motors electronically allowing one to ascertain the position and the orientation of the electron beam.	30
5	Two-dimensional geometry of a separator magnet.	31

6	Decay of the normalized field B/B_0 as a function of the gap distance between the pole plates $2h$ for the separator magnet with a width of the grooves $2a$ of 3 mm. The decay and thus the overlap of perturbations to the magnetic fields of two adjacent grooves will be reduced considerably when the gap is reduced from seven to five millimeters. By the same token, the distance to the point where the groove is beginning to bend appreciably χ , measured in units of the half-gap distance h , increases. Since the groove distances and curvatures of corresponding optimized solutions remain approximately the same, the parameter χ/h scales with the reciprocal gap distance. Thus, the perturbations of the curved portion of the groove to the magnetic field in the region close to the beam path is substantially diminished, because of the strong dependence of the normalized magnetic field B/B_0 on $r = a/h$ (See Equation 1).	32
7	Resolution computed for a distribution consisting of 27000 electrons at the image plane of the separator originating from a sample with a work function of 5 eV after traversing a perfect front end with a magnification of -12 and an accelerating voltage of 20 kV as a function of the field size in the x - z section. The three curves show the resolution as a function of the radius of the field of view for separators differing in the half-distance h of the pole plates. Each of these separator designs was optimized when the gap was altered to the figure indicated. Thus, these designs differ in the groove positions and orientations. The difference in the optical properties of the separators shown is negligible.	33
8	This graph shows the resolution as a function of the radius of the field of view for the y - z section for the same setup as in Figure 7.	34
9	Change in the field of view for different symmetric perturbations of the center groove after employing the correction scheme utilizing the three internal correctors currents and the distance of the image plane from the edge of separator as variables ¹ , while fitting for a stigmatic image at the 45° (S_1 -) plane and a zero slope of the dispersion ray $x'_\kappa(z_{S_1})$ at the remaining symmetry plane (S_1). Here the resolutions obtained in the x - z section are shown. We were unable to obtain a solution for a misalignment of more than -2.8320 mrad.	35
10	Same as in the previous figure 9, but for the y - z imaging section.	36

11	Random errors before correction. A Gaussian random number generator was employed for generating alignment errors $\sigma_{x,y} = 25 \mu\text{m}$ for the positions and $\sigma_\phi = 1 \text{ mrad}$ for the orientations. An ensemble of 100 misaligned separators was used for preparing the plot data.	37
12	Relative corrector strengths for the six correction elements. A Gaussian random number generator was employed for generating alignment errors $\sigma_{x,y} = 25 \mu\text{m}$ for the positions and $\sigma_\phi = 1 \text{ mrad}$ for the orientations. An ensemble of 100 misaligned separators was used for preparing the plot data. .	38
13	Axial resolutions before and after correction. A Gaussian random number generator was employed for generating alignment errors $\sigma_{x,y} = 25 \mu\text{m}$ for the positions and $\sigma_\phi = 1 \text{ mrad}$ for the orientations. An ensemble of 100 misaligned separators was used for preparing the plot data.	39
14	Off-axial resolution computed for the point $(-5 \mu\text{m}, -5 \mu\text{m})$ on the sample before and after correction. A Gaussian random number generator was employed for generating alignment errors $\sigma_{x,y} = 25 \mu\text{m}$ for the positions and $\sigma_\phi = 1 \text{ mrad}$ for the orientations. An ensemble of 100 misaligned separators was used for preparing the plot data.	40
15	Displacement before and after correction. A Gaussian random number generator was employed for generating alignment errors $\sigma_{x,y} = 25 \mu\text{m}$ for the positions and $\sigma_\phi = 1 \text{ mrad}$ for the orientations. An ensemble of 100 misaligned separators was used for preparing the plot data.	41
16	Off-axial linear matrix elements as a function of the axial resolution computed for an ensemble of 500 perturbed separators.	42
17	Diagonal linear matrix elements as a function of the axial resolution computed for an ensemble of 500 perturbed separators.	43

- 18 The axial resolution of a system consisting of the objective, field, and transfer lenses for two different aperture radii is shown. The correction utilizes the six internal correctors, as used for correcting a single pass through the separator shown earlier, and additionally three electrostatic and two magnetic dipole fields for orbit correction in combination with two electrostatic quadrupole fields for correcting linear focusing errors. An ensemble of 500 misaligned separators with a specification of $\sigma_{x,y} = 10 \mu\text{m}$ and $\sigma_\phi = 0.5 \text{ mrad}$ in an otherwise perfectly aligned system was chosen. All aberration terms through fourth rank are included. The green lines indicate the nominal value for a setup free of imperfections. The red lines border a σ environment centered on the mean value drawn as a blue line. The plots show a separator with the given specification is correctable for an axial point. 44
- 19 This resolution vs transmission plot, for the ensemble of 500 misaligned separators used for obtaining the plots in Figure 18, depicts the remaining deviations from the curve for a perfectly setup PEEM3 (drawn in red) after correction for errors for four different aperture radii. 45

List of Tables

I	Figures for the field decay of the normalized magnetic field B/B_0 generated by the arrangement shown in Figure 5 as a function of the ratio of the distance from the center of the groove χ to the half gap distance $h = D/2$. Reducing h , while keeping the half groove width $a = S/2$ fixed, results in a larger χ/h at the location of an adjacent groove or beginning of groove curvature. Therefore, deviation from the model due to either an adjacent groove curvature is substantially decreased.	47
II	A change in the half distance h between the pole pieces, causes a different optimal solution for the layout when we fit for a double-symmetric solution with a total bending angle of 90° . Here is shown how the distance between adjacent groove positions g1–g2 and g2–g3, respectively, taken as the point of intersection of the trajectory and the groove, change when the distance between the pole plate changes. A beam energy of 20 kV and grooves with an equal width of 3 mm were assumed.	48
III	Change of the optimal groove orientations as a function of the gap width. . .	49
IV	Change of the optimal current as a function of the gap width.	50

Figures

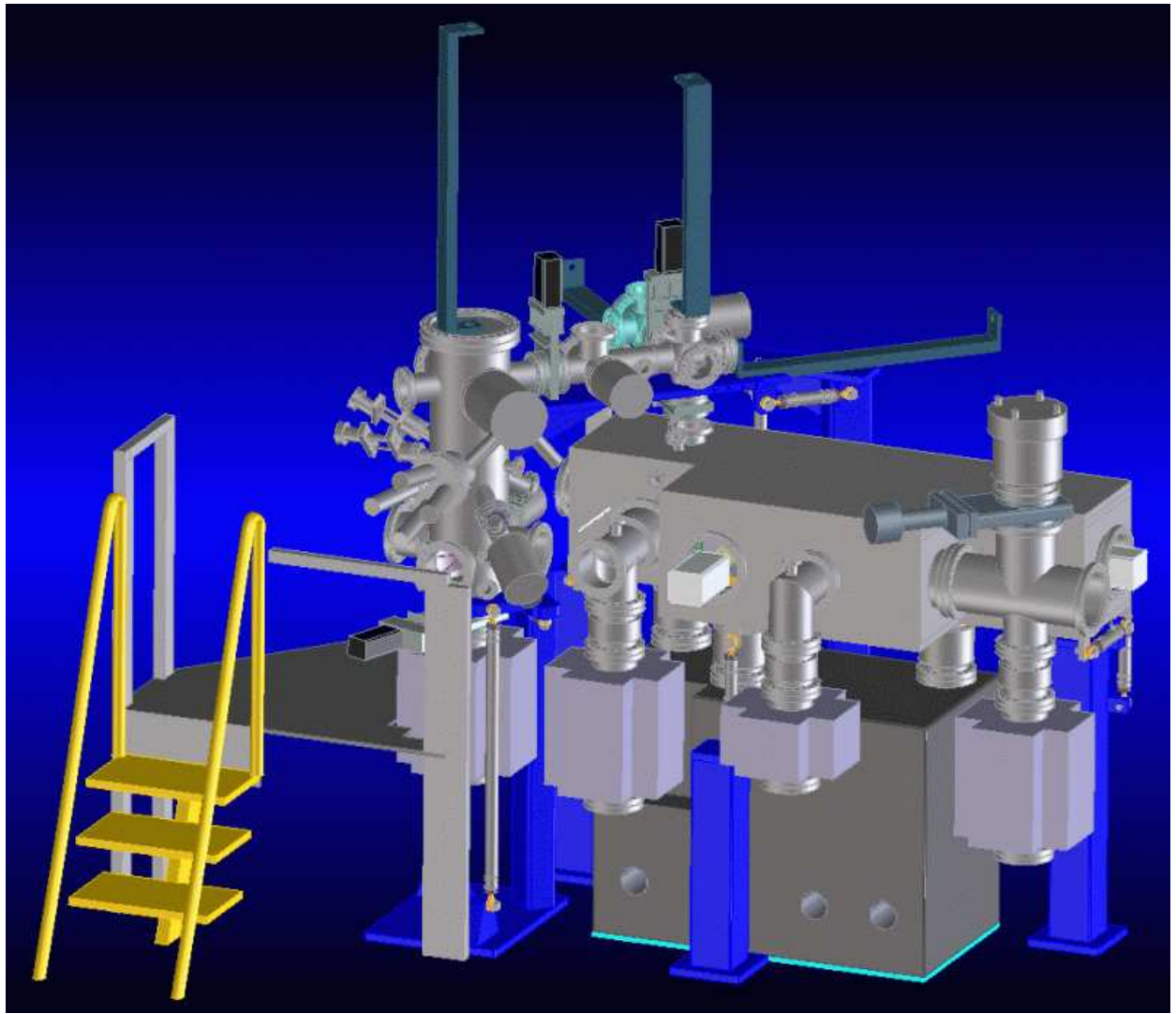


FIG. 1: Full view of the PEEM3 spectromicroscope.

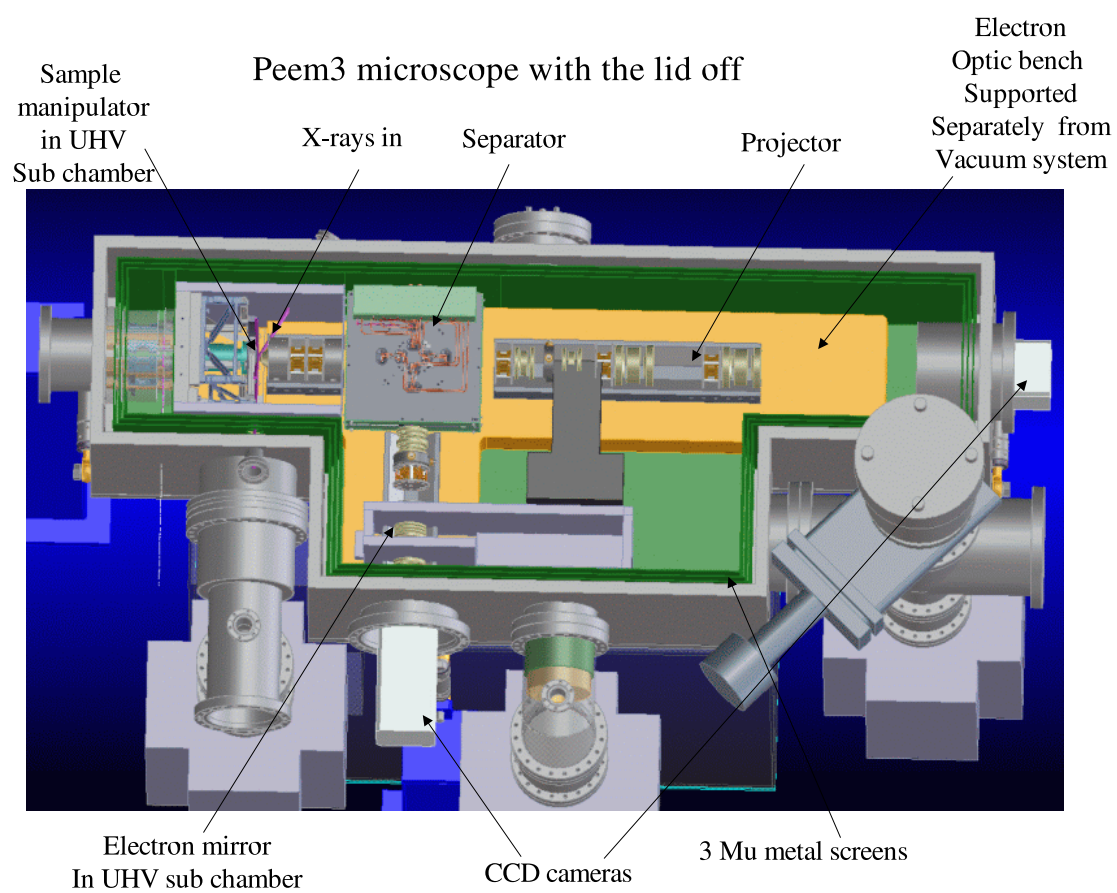


FIG. 2: The components of the PEEM3 microscope.

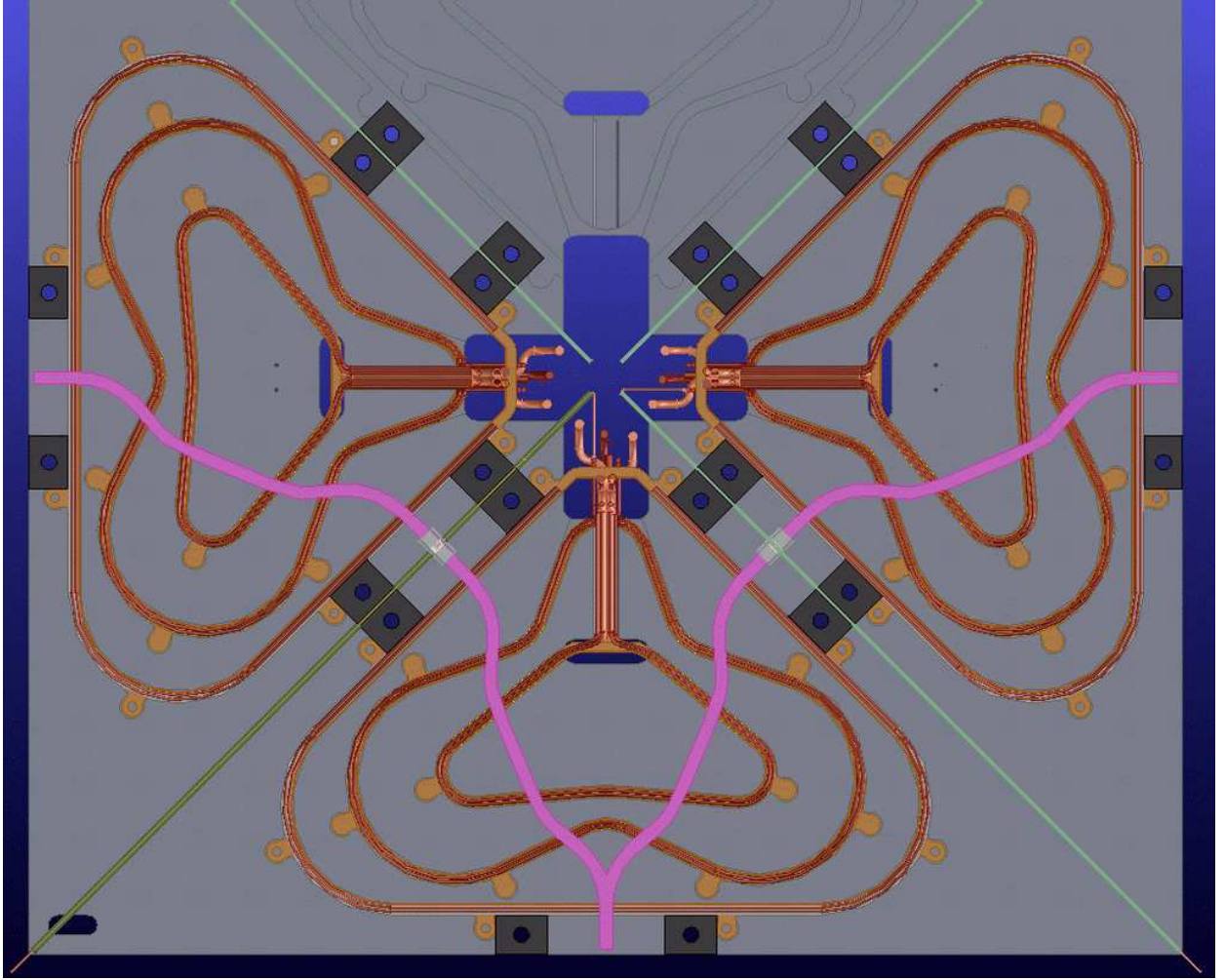


FIG. 3: Layout of the separator windings. The double-symmetric layout is clearly visible. Vertical and horizontal dipole elements are located at the 45° planes, intended for checking the location of the image planes.

Alignment layout scheme – P E E M 3

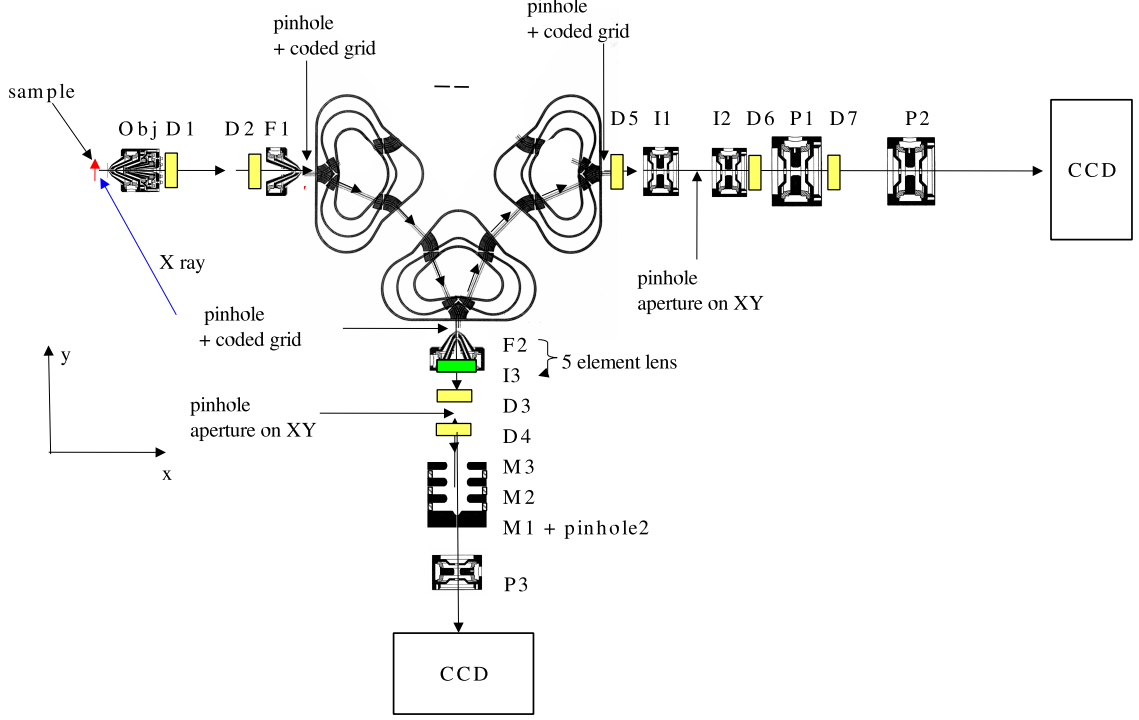


FIG. 4: Schematic layout of PEEM3. All of the correction and monitoring facilities are indicated. Such as the 90° PEEM facility provided in the mirror column, consisting of the modified field lens F_2 , the mirror, the additional lens P_3 and a separate CCD camera. For external correction, there are the electrostatic dodecapole elements D_1 through D_7 which can be employed to generate dipole, quadrupole, hexapole and octopole fields to correct for parasitic aberrations. In order to influence the impinging and the reflected beam independently utilizing the velocity dependence of the magnetic component of the Lorentz force, the elements D_3 and D_4 are combined electrostatic and magnetic twelve-pole elements. At the exit and the entry faces of the separator there are coded grids and pinholes which can be moved by motors electronically allowing one to ascertain the position and the orientation of the electron beam.

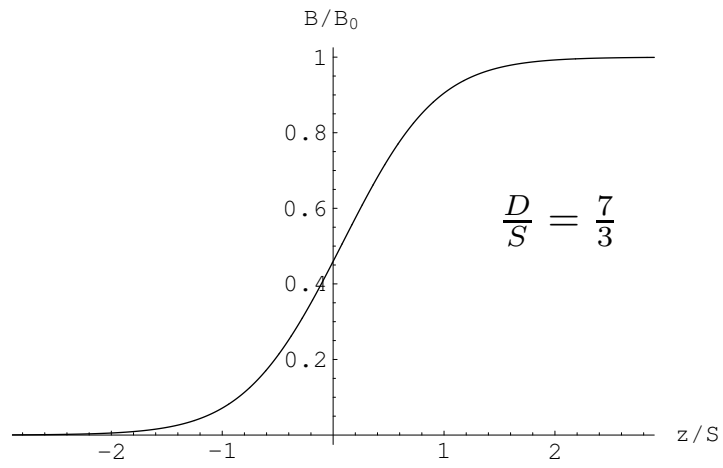
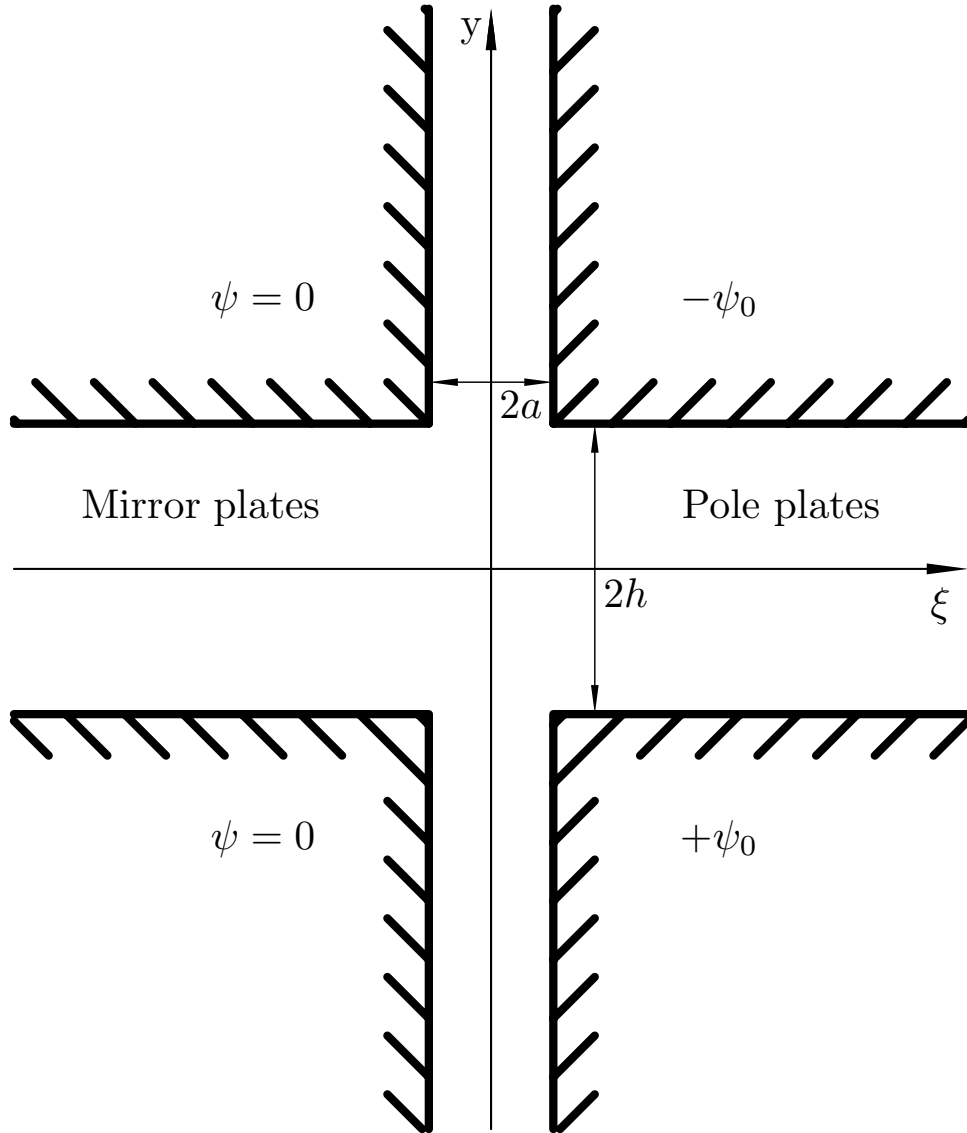


FIG. 5: Two-dimensional geometry of a separator magnet.

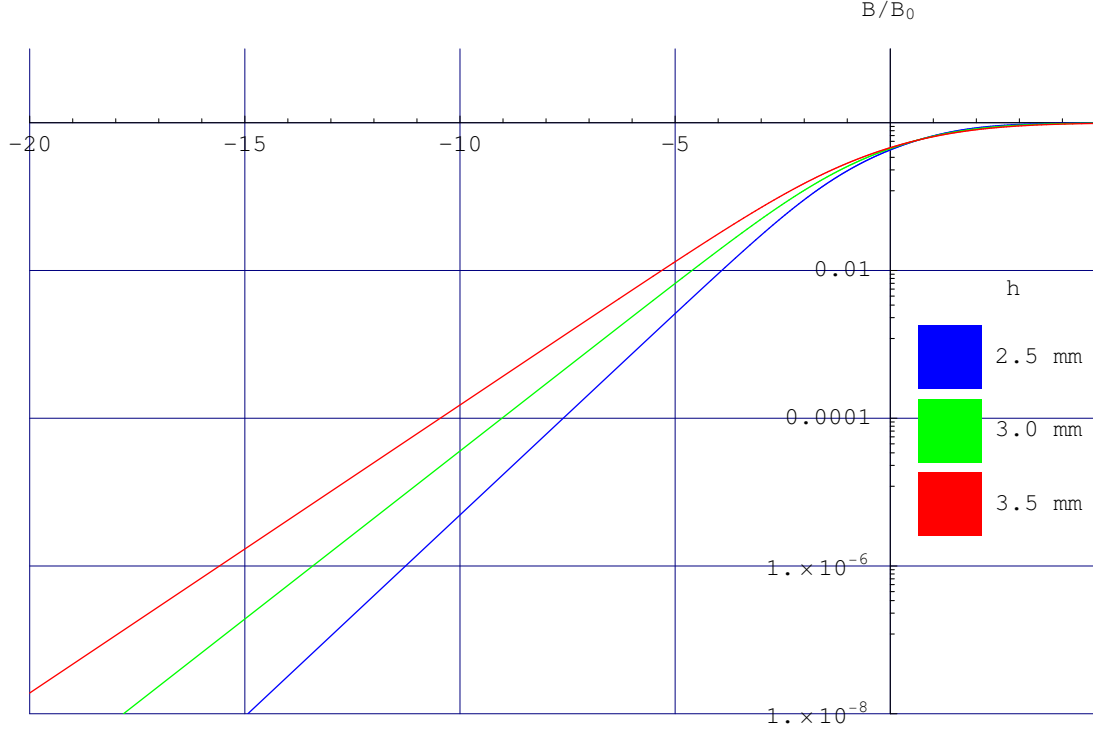


FIG. 6: Decay of the normalized field B/B_0 as a function of the gap distance between the pole plates $2h$ for the separator magnet with a width of the grooves $2a$ of 3 mm. The decay and thus the overlap of perturbations to the magnetic fields of two adjacent grooves will be reduced considerably when the gap is reduced from seven to five millimeters. By the same token, the distance to the point where the groove is beginning to bend appreciably χ , measured in units of the half-gap distance h , increases. Since the groove distances and curvatures of corresponding optimized solutions remain approximately the same, the parameter χ/h scales with the reciprocal gap distance. Thus, the perturbations of the curved portion of the groove to the magnetic field in the region close to the beam path is substantially diminished, because of the strong dependence of the normalized magnetic field B/B_0 on $r = a/h$ (See Equation 1).

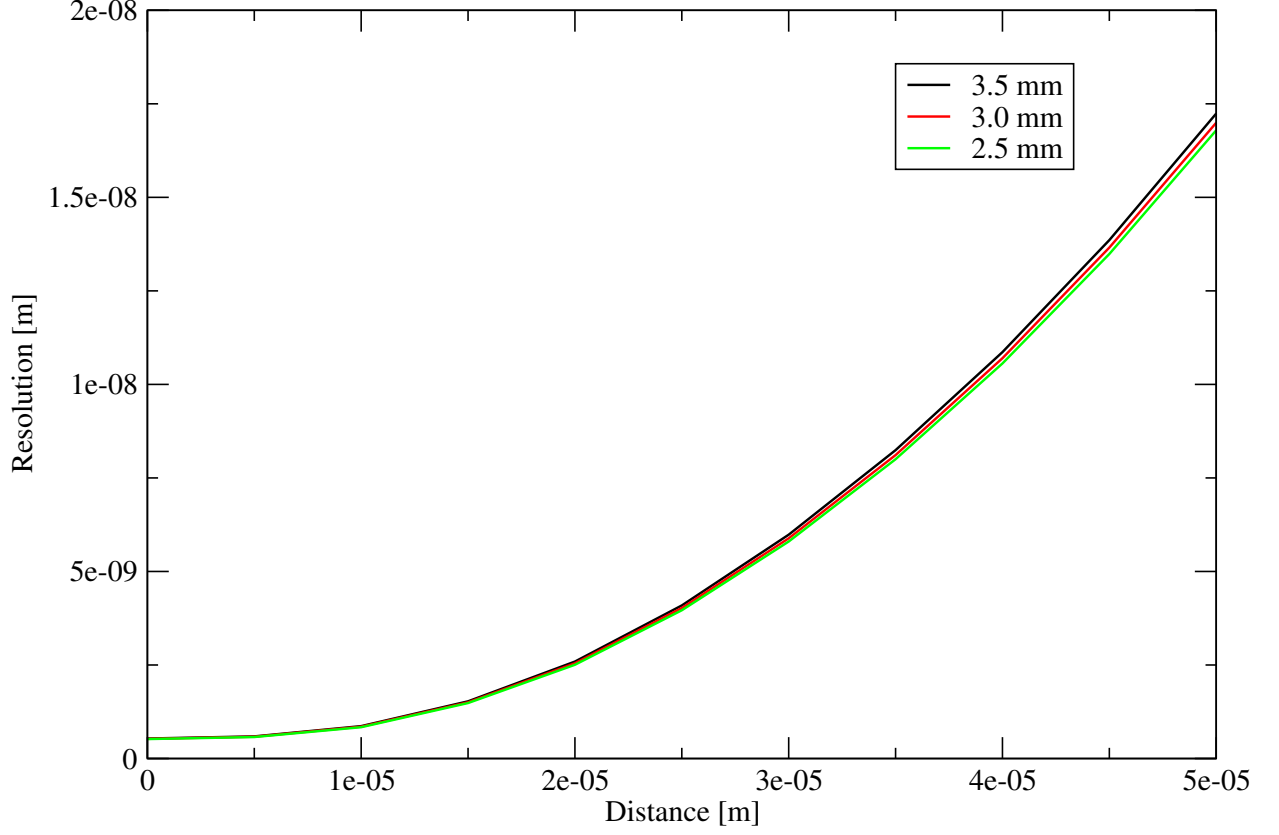


FIG. 7: Resolution computed for a distribution consisting of 27000 electrons at the image plane of the separator originating from a sample with a work function of 5 eV after traversing a perfect front end with a magnification of -12 and an accelerating voltage of 20 kV as a function of the field size in the x - z section. The three curves show the resolution as a function of the radius of the field of view for separators differing in the half-distance h of the pole plates. Each of these separator designs was optimized when the gap was altered to the figure indicated. Thus, these designs differ in the groove positions and orientations. The difference in the optical properties of the separators shown is negligible.

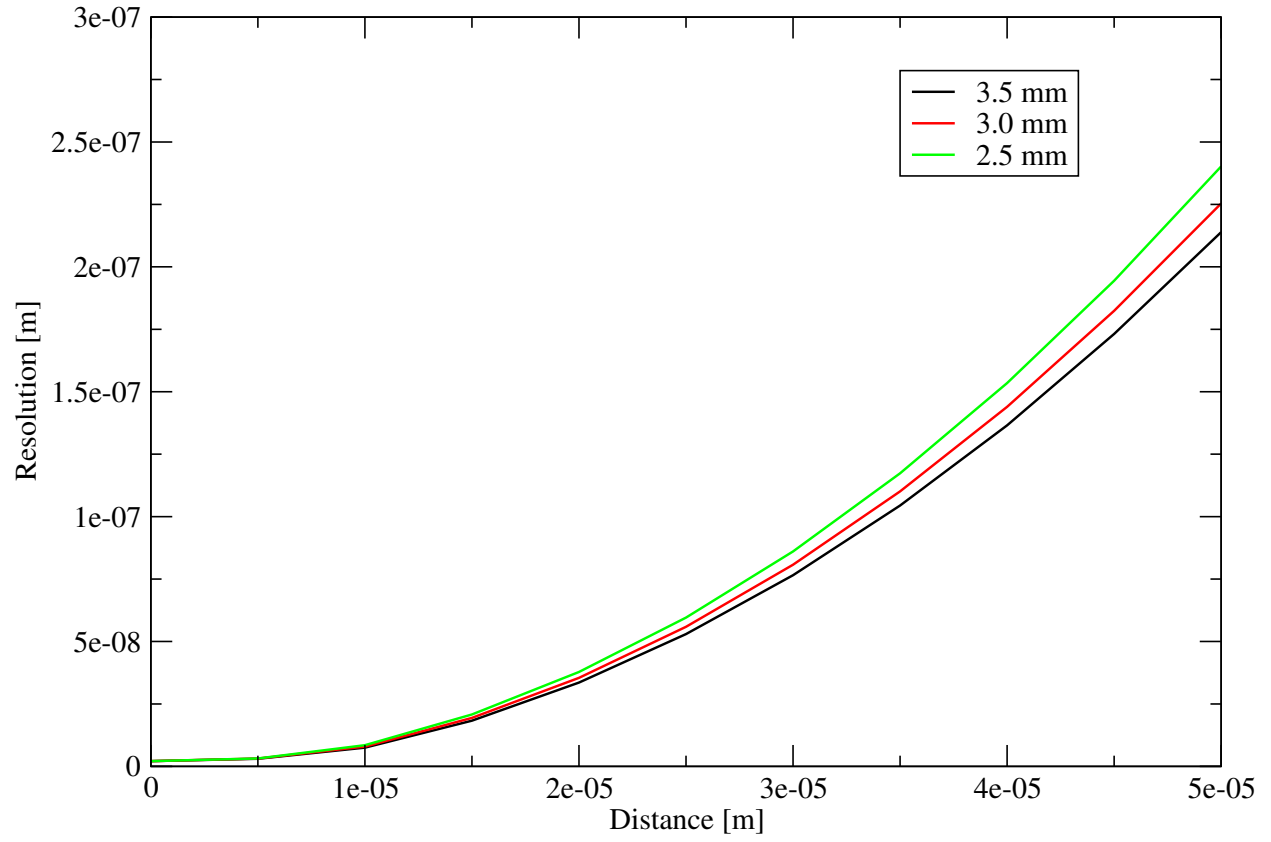


FIG. 8: This graph shows the resolution as a function of the radius of the field of view for the y - z section for the same setup as in Figure 7.

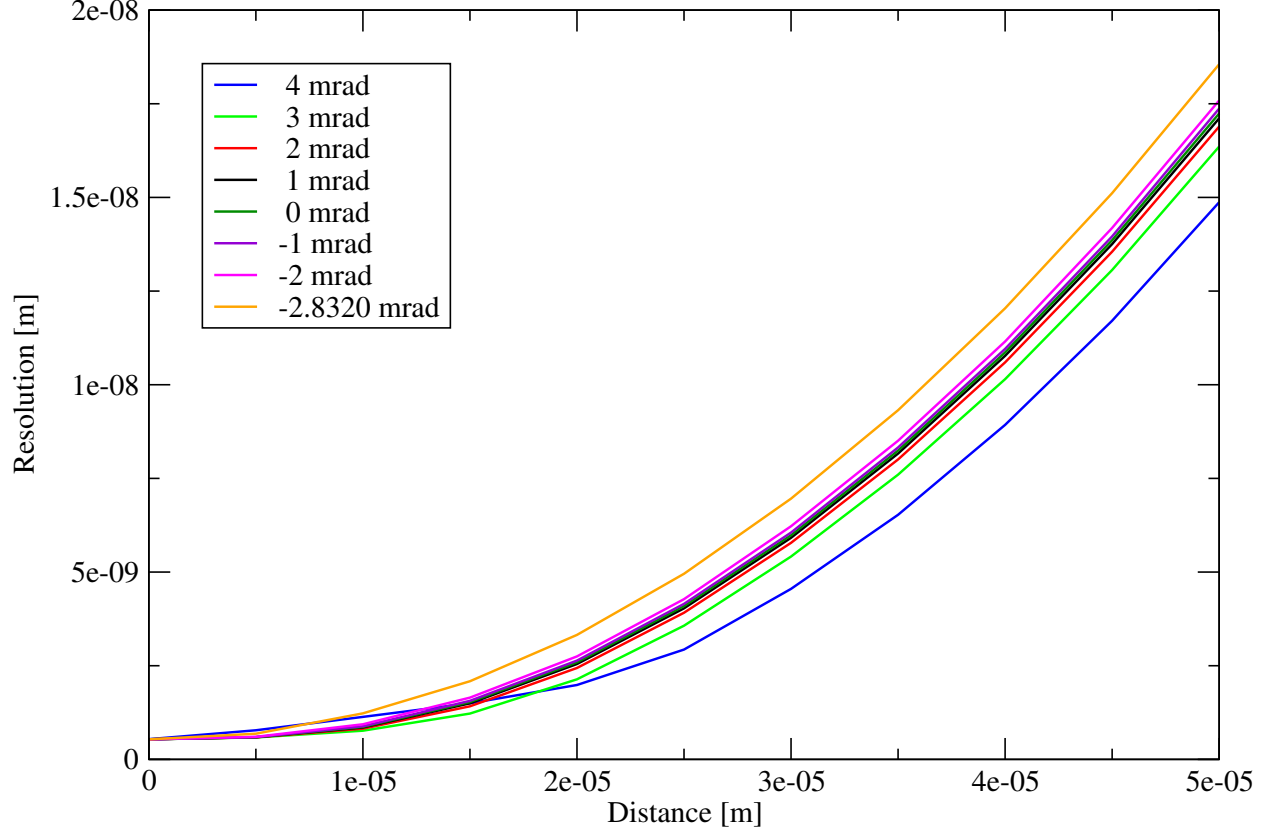


FIG. 9: Change in the field of view for different symmetric perturbations of the center groove after employing the correction scheme utilizing the three internal correctors currents and the distance of the image plane from the edge of separator as variables1, while fitting for a stigmatic image at the 45° (S_{1-}) plane and a zero slope of the dispersion ray $x'_\kappa(z_{S_1})$ at the remaining symmetry plane (S_1). Here the resolutions obtained in the x - z section are shown. We were unable to obtain a solution for a misalignment of more than -2.8320 mrad.

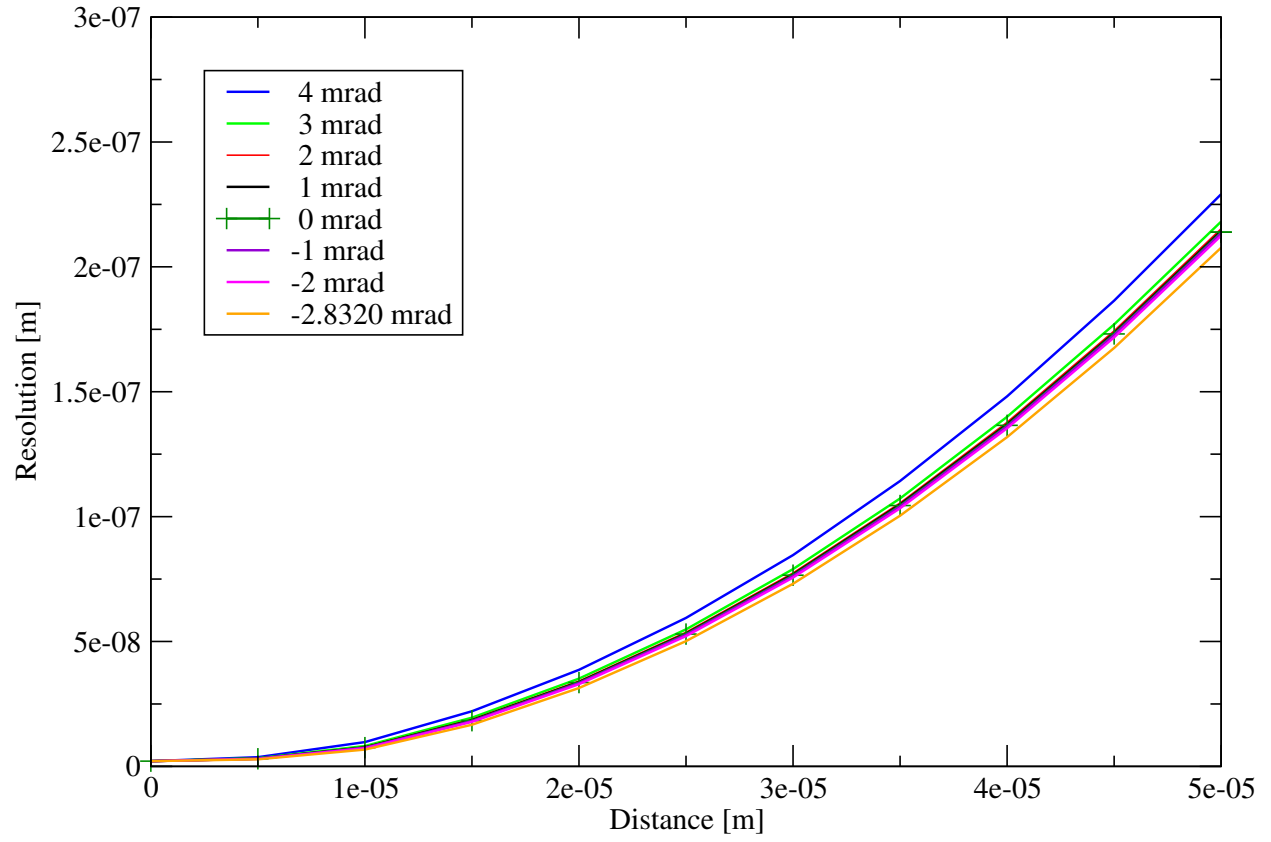
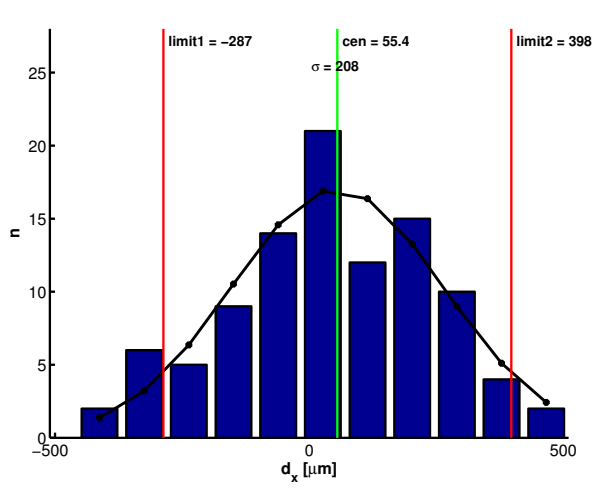
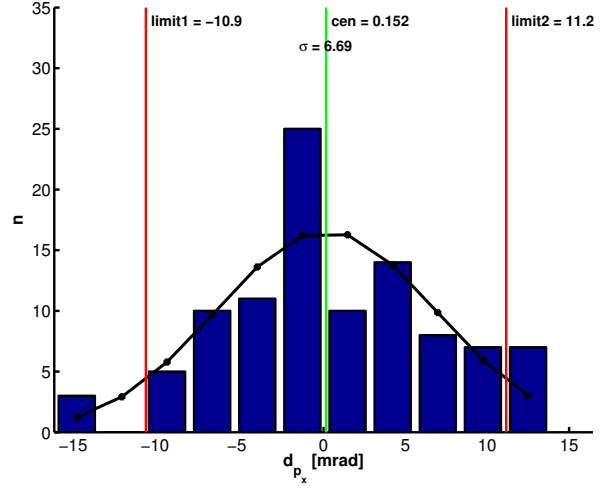


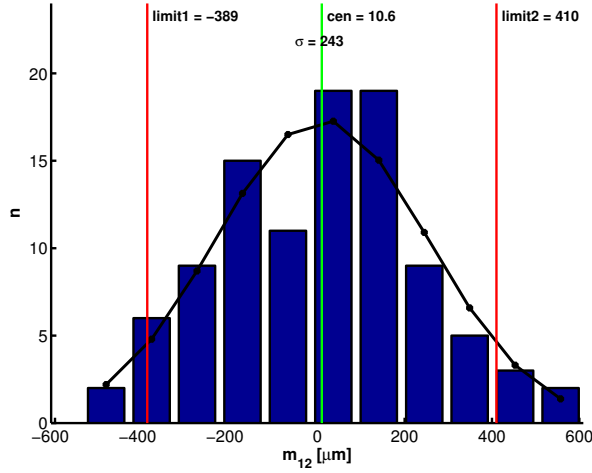
FIG. 10: Same as in the previous figure 9, but for the y - z imaging section.



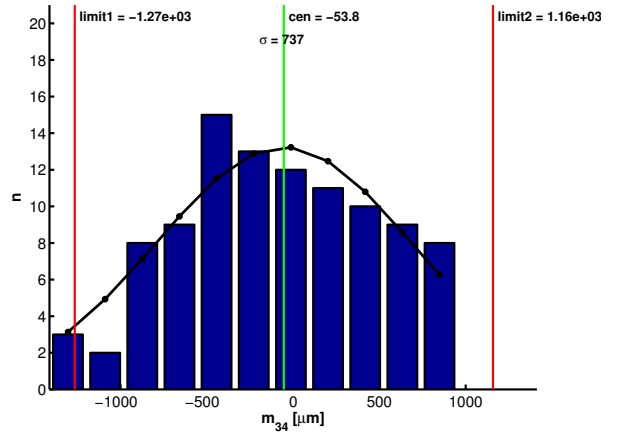
(a) Dispersion d_x



(b) Angular dispersion d_{p_x}



(c) m_{12}



(d) m_{34}

FIG. 11: Random errors before correction. A Gaussian random number generator was employed for generating alignment errors $\sigma_{x,y} = 25 \mu\text{m}$ for the positions and $\sigma_\phi = 1 \text{ mrad}$ for the orientations. An ensemble of 100 misaligned separators was used for preparing the plot data.

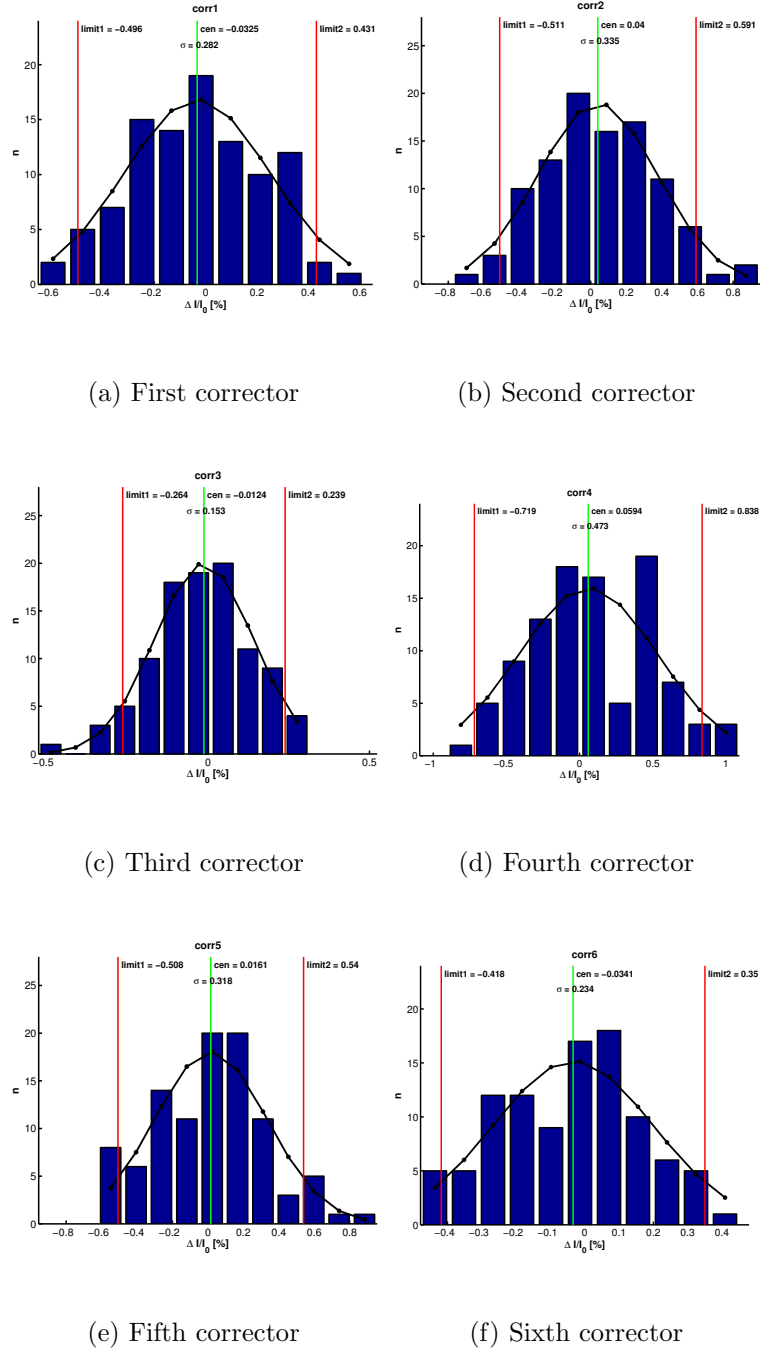
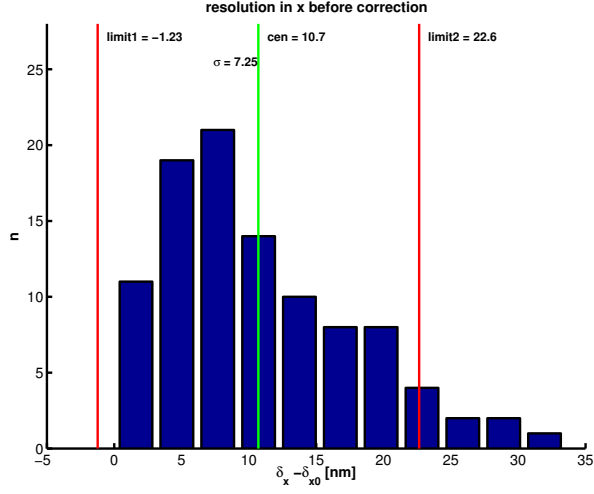
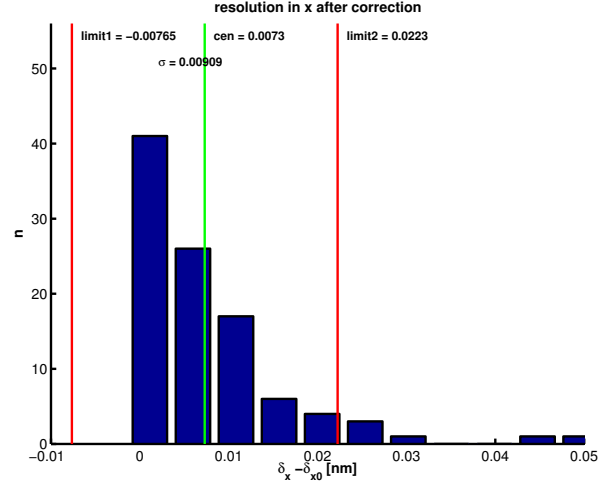


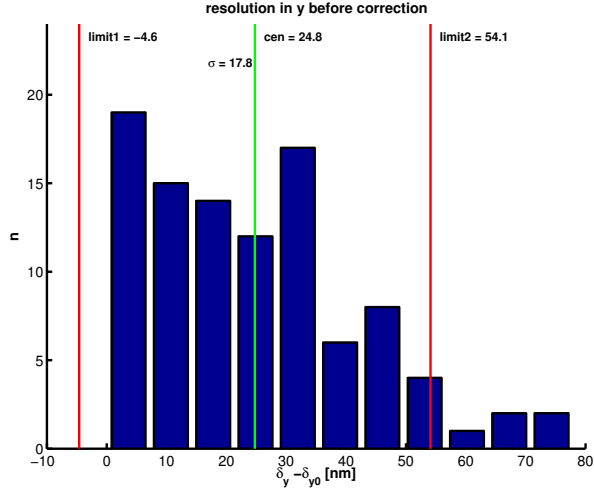
FIG. 12: Relative corrector strengths for the six correction elements. A Gaussian random number generator was employed for generating alignment errors $\sigma_{x,y} = 25 \mu\text{m}$ for the positions and $\sigma_\phi = 1 \text{ mrad}$ for the orientations. An ensemble of 100 misaligned separators was used for preparing the plot data.



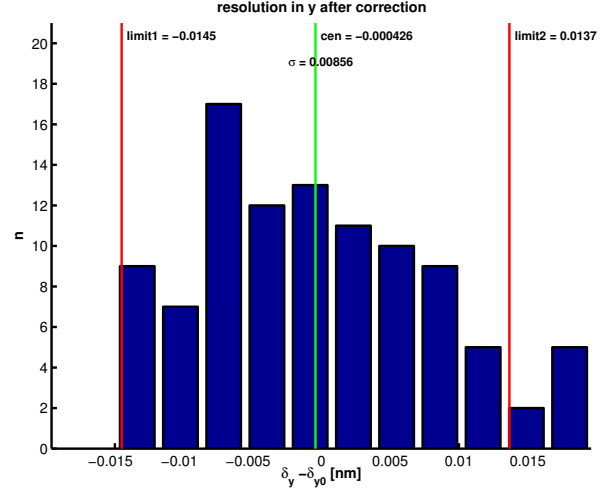
(a) Resolution in the x - z section before
correction



(b) Resolution in the x - z section after
correction

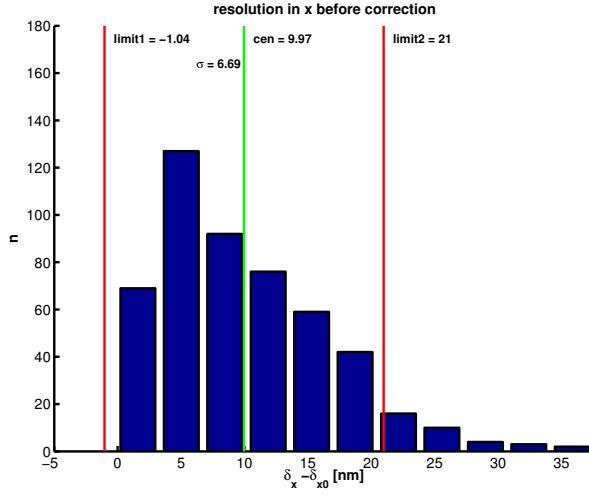


(c) Resolution in the y - z section before
correction

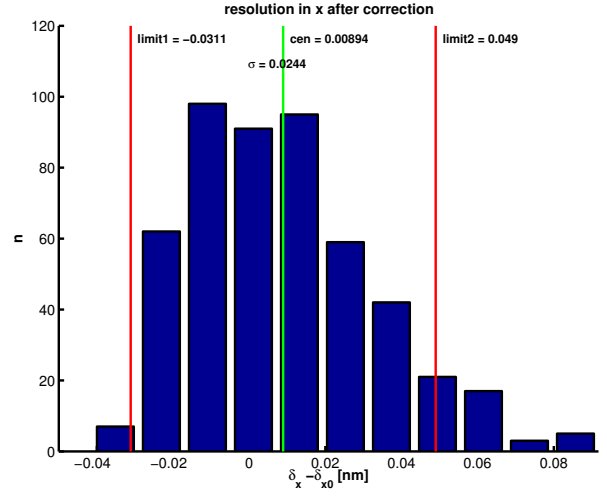


(d) Resolution in the y - z section after
correction

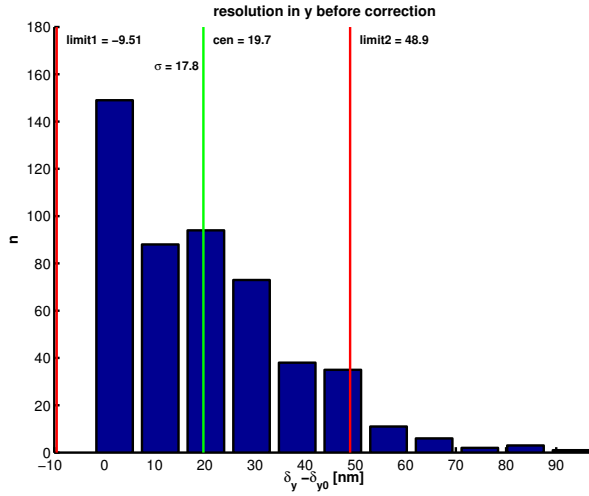
FIG. 13: Axial resolutions before and after correction. A Gaussian random number generator was employed for generating alignment errors $\sigma_{x,y} = 25 \mu\text{m}$ for the positions and $\sigma_\phi = 1 \text{ mrad}$ for the orientations. An ensemble of 100 misaligned separators was used for preparing the plot data.



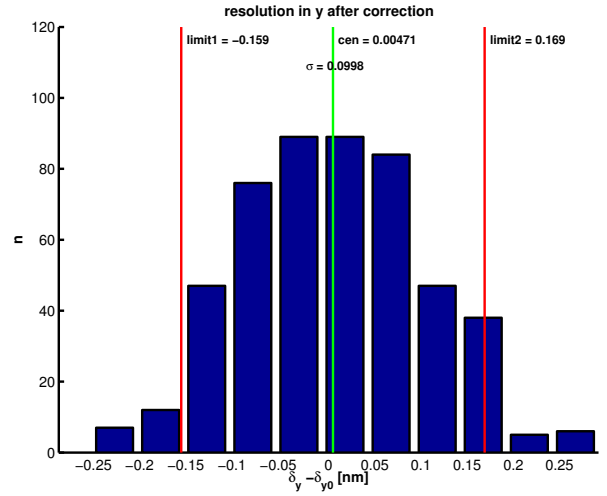
(a) Resolution in the x - z section before correction



(b) Resolution in the x - z section after correction



(c) Resolution in the y - z section before correction



(d) Resolution in the y - z section after correction

FIG. 14: Off-axial resolution computed for the point $(-5\mu\text{m}, -5\mu\text{m})$ on the sample before and after correction. A Gaussian random number generator was employed for generating alignment errors $\sigma_{x,y} = 25\mu\text{m}$ for the positions and $\sigma_\phi = 1\text{mrad}$ for the orientations. An ensemble of 100 misaligned separators was used for preparing the plot data.

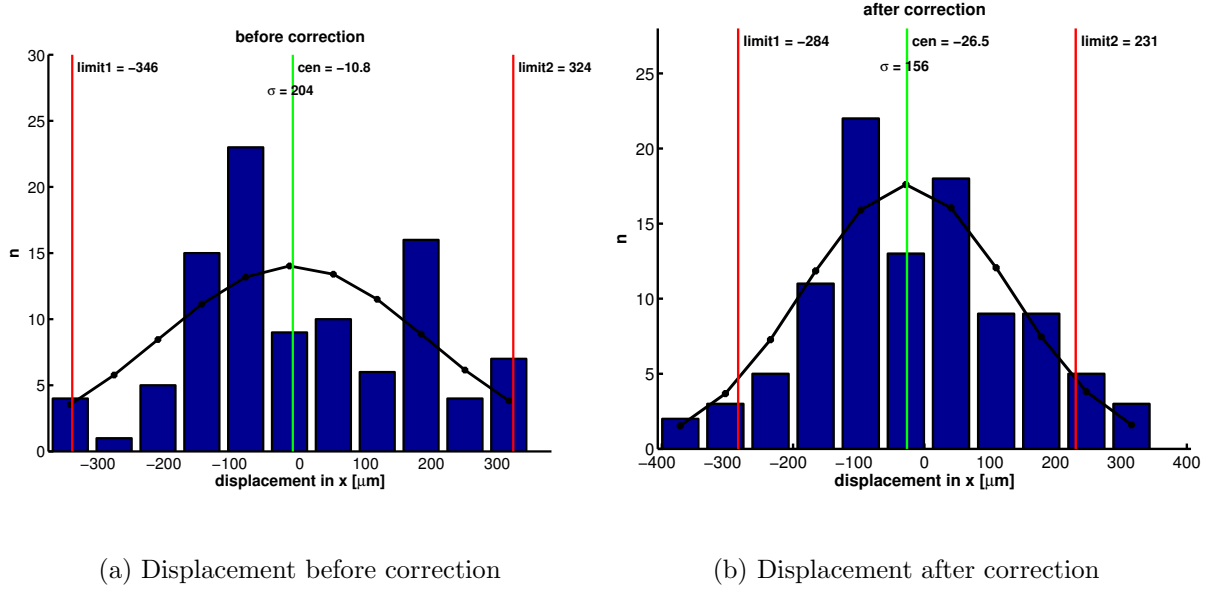


FIG. 15: Displacement before and after correction. A Gaussian random number generator was employed for generating alignment errors $\sigma_{x,y} = 25 \mu\text{m}$ for the positions and $\sigma_\phi = 1 \text{ mrad}$ for the orientations. An ensemble of 100 misaligned separators was used for preparing the plot data.

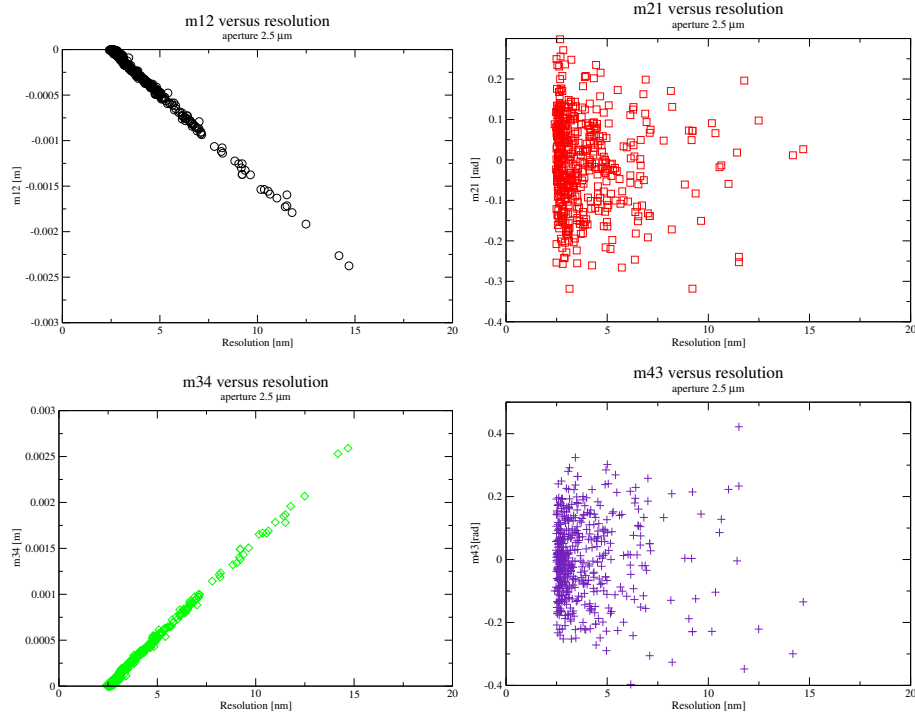


FIG. 16: Off-axial linear matrix elements as a function of the axial resolution computed for an ensemble of 500 perturbed separators.

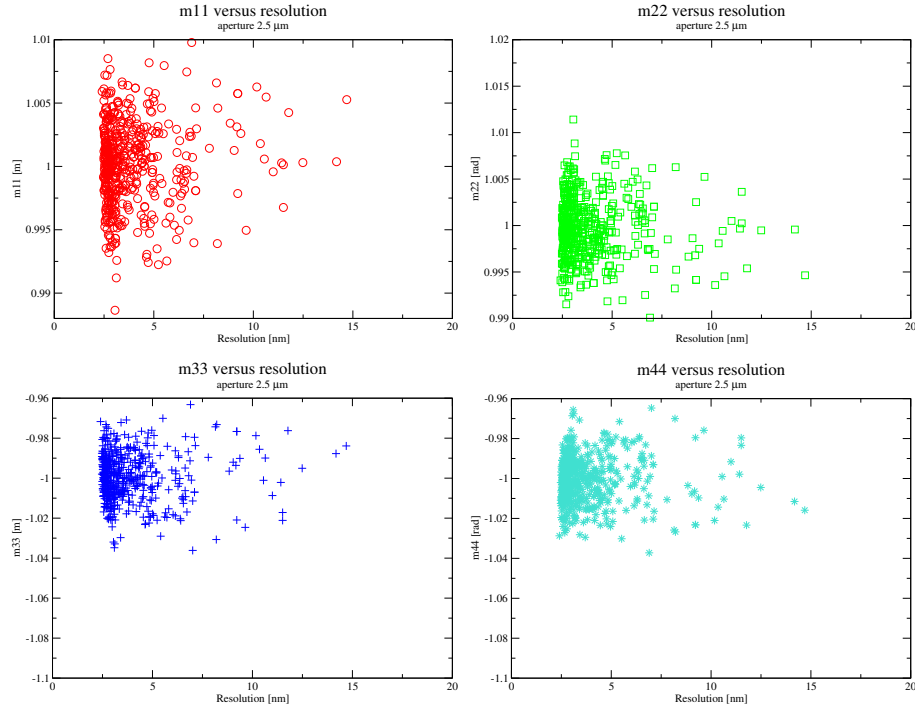


FIG. 17: Diagonal linear matrix elements as a function of the axial resolution computed for an ensemble of 500 perturbed separators.

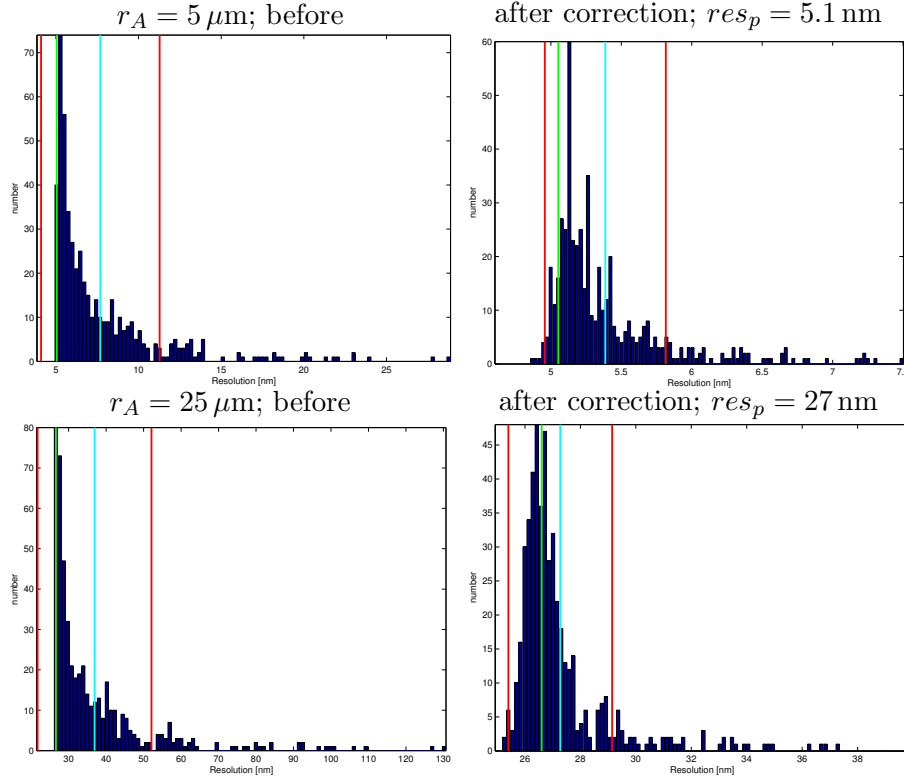


FIG. 18: The axial resolution of a system consisting of the objective, field, and transfer lenses for two different aperture radii is shown. The correction utilizes the six internal correctors, as used for correcting a single pass through the separator shown earlier, and additionally three electrostatic and two magnetic dipole fields for orbit correction in combination with two electrostatic quadrupole fields for correcting linear focusing errors. An ensemble of 500 misaligned separators with a specification of $\sigma_{x,y} = 10 \mu\text{m}$ and $\sigma_\phi = 0.5 \text{ mrad}$ in an otherwise perfectly aligned system was chosen. All aberration terms through fourth rank are included. The green lines indicate the nominal value for a setup free of imperfections. The red lines border a σ environment centered on the mean value drawn as a blue line. The plots show a separator with the given specification is correctable for an axial point.

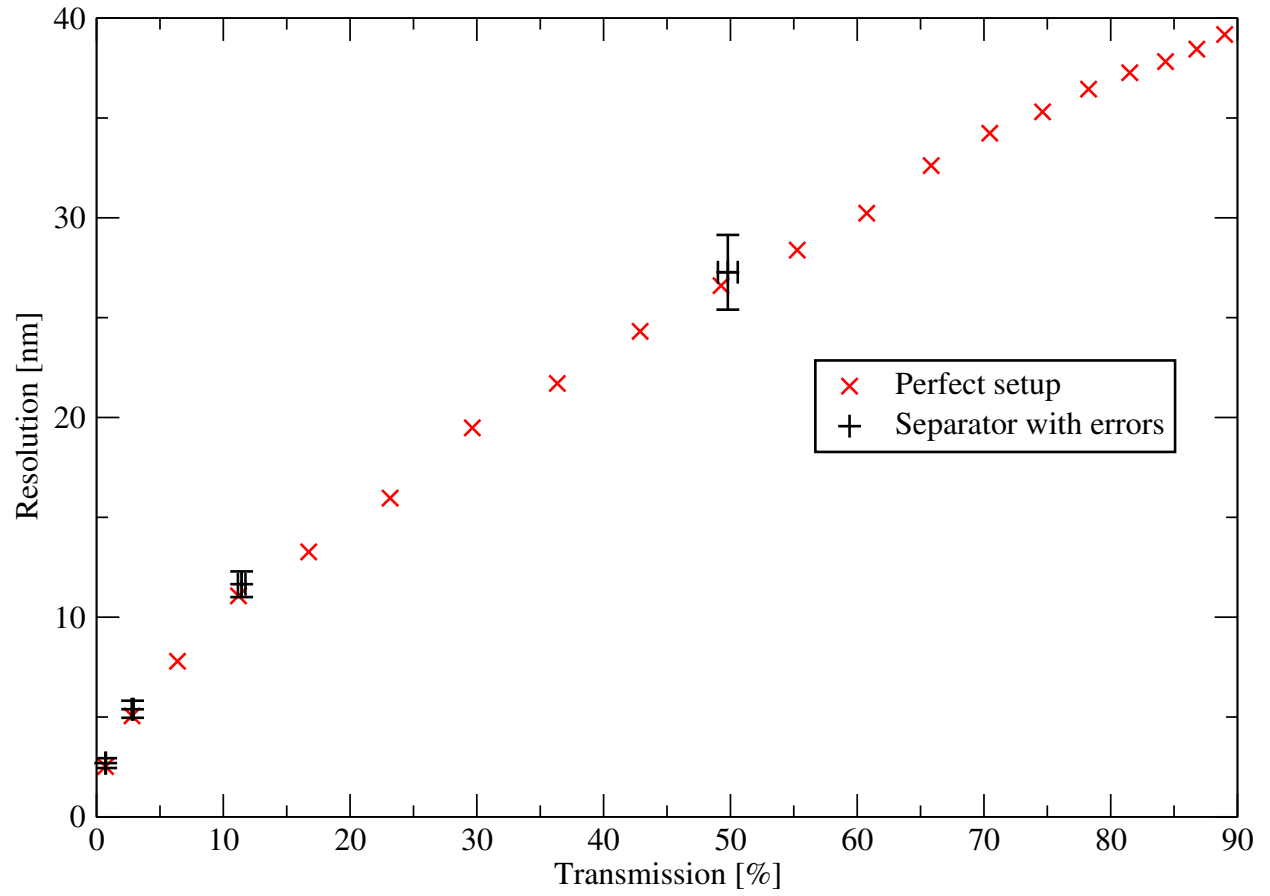


FIG. 19: This resolution vs transmission plot, for the ensemble of 500 misaligned separators used for obtaining the plots in Figure 18, depicts the remaining deviations from the curve for a perfectly setup PEEM3 (drawn in red) after correction for errors for four different aperture radii.

Tables

$\frac{B}{B_0}$	$\frac{\chi}{h}$
10^{-4}	-3.0
10^{-5}	-3.7
10^{-6}	-4.5

TABLE I: Figures for the field decay of the normalized magnetic field B/B_0 generated by the arrangement shown in Figure 5 as a function of the ratio of the distance from the center of the groove χ to the half gap distance $h = D/2$. Reducing h , while keeping the half groove width $a = S/2$ fixed, results in a larger χ/h at the location of an adjacent groove or beginning of groove curvature. Therefore, deviation from the model due to either an adjacent groove curvature is substantially decreased.

distance	$h = 2.5 \text{ mm}$	$h = 3.0 \text{ mm}$	$h = 3.5 \text{ m}$
g1–g2	0.0198604 m	0.0196313 m	0.0193971 m
g2–g3	0.0126625 m	0.0125734 m	0.0124933 m

TABLE II: A change in the half distance h between the pole pieces, causes a different optimal solution for the layout when we fit for a double-symmetric solution with a total bending angle of 90° . Here is shown how the distance between adjacent groove positions g1–g2 and g2–g3, respectively, taken as the point of intersection of the trajectory and the groove, change when the distance between the pole plate changes. A beam energy of 20 kV and grooves with an equal width of 3 mm were assumed.

angle	$h = 2.5$ mm	$h = 3.0$ mm	$h = 3.5$ mm
ϕ_1	0.000000 rad	0.000000 rad	0.000000 rad
ϕ_2	0.445496 rad	0.435293 rad	0.424233 rad
ϕ_3	0.0883988 rad	0.0867050 rad	0.0848109 rad

TABLE III: Change of the optimal groove orientations as a function of the gap width.

current	$h = 2.5 \text{ mm}$	$h = 3.0 \text{ mm}$	$h = 3.5 \text{ mm}$
I	47.6812 A	58.2947 A	69.4333 A

TABLE IV: Change of the optimal current as a function of the gap width.